JGR Space Physics

RESEARCH ARTICLE
10.1029/2024JA032660

3D Simulation of an Extreme SAID Flow Channel

Joaquín Díaz Peña[1], **Matthew Zettergren**[2], **Joshua Semeter**[1], **Yukitoshi Nishimura**[1], **Michael Hirsch**[1], **and Brian M. Walsh**[3]

[1]Department of Electrical Engineering and Center for Space Physics, Boston University, Boston, MA, USA, [2]Department of Physical Sciences, Embry-Riddle Aeronautical University, Daytona Beach, FL, USA, [3]Department of Mechanical Engineering and Center for Space Physics, Boston University, Boston, MA, USA

Key Points:

- We present a full 4D (3D + time) simulation of an extreme SAID
- We utilize the GEMINI model for the simulation due to the practicality and easiness to set arbitrary input files. Though challenges remain
- We highlight the importance of inelastic collisions and impact ionization on damping the channel velocity, physics not included in GEMINI

Supporting Information:

Supporting Information may be found in the online version of this article.

Correspondence to:

J. Díaz Peña,
jmdp@bu.edu

Citation:

Díaz Peña, J., Zettergren, M., Semeter, J., Nishimura, Y., Hirsch, M., & Walsh, B. M. (2024). 3D simulation of an extreme SAID flow channel. *Journal of Geophysical Research: Space Physics*, *129*, e2024JA032660. https://doi.org/10.1029/2024JA032660

Received 20 MAR 2024
Accepted 12 JUN 2024

Author Contributions:

Conceptualization: Joaquín Díaz Peña, Joshua Semeter
Data curation: Matthew Zettergren, Yukitoshi Nishimura, Michael Hirsch
Formal analysis: Joaquín Díaz Peña, Matthew Zettergren, Joshua Semeter
Funding acquisition: Brian M. Walsh
Investigation: Joaquín Díaz Peña
Methodology: Joaquín Díaz Peña
Resources: Joshua Semeter
Software: Joaquín Díaz Peña, Matthew Zettergren, Michael Hirsch
Supervision: Matthew Zettergren, Joshua Semeter, Yukitoshi Nishimura
Validation: Matthew Zettergren, Joshua Semeter, Yukitoshi Nishimura
Visualization: Joaquín Díaz Peña
Writing – original draft: Joaquín Díaz Peña
Writing – review & editing: Joaquín Díaz Peña, Joshua Semeter, Brian M. Walsh

Abstract Space-based observations of the signatures associated with STEVE show how this phenomenon might be closely related to an extreme version of a SAID channel. Measurements show high velocities (>4 km/s), high temperatures (>4,000 K), and very large current density drivers (up to 1 μA/m^2). This phenomena happens in a small range of latitudes, less than a degree, but with a large longitudinal span. In this study, we utilize the GEMINI model to simulate an extreme SAID/STEVE. We assume a FAC density coming from the magnetosphere as the main driver, allowing all other parameters to adjust accordingly. We have two main objectives with this work: show how an extreme SAID can have velocity values comparable or larger than the ones measured under STEVE, and to display the limitations and missing physics that arise due to the extreme values of temperature and velocity. Changes had to be made to GEMINI due to the extreme conditions, particularly some neutral-collision frequencies. The importance of the temperature threshold at which some collision frequencies go outside their respective bounds, as well as significance of the energies that would cause inelastic collisions and impact ionization are displayed and discussed. We illustrate complex structures and behaviors, emphasizing the importance of 3D simulations in capturing these phenomena. Longitudinal structure is emphasized, as the channel develops differently depending on MLT. However, these simulations should be viewed as approximations due to the limited observations available to constrain the model inputs and the assumptions made to achieve sensible results.

1. Introduction

Ionospheric flow channels, characterized by fast, localized plasma flows, significantly influence the dynamics and structure of the ionosphere (Lyons et al., 2016). They affect the distribution of ionospheric plasma, the transport of energy and momentum, and the coupling of the ionosphere with the magnetosphere and the atmosphere (Nishimura et al., 2021). Subauroral Ion Drift (SAID) flow channels, a specific type of flow channel occurring in the subauroral region of the ionosphere, are narrow latitudinal channels of fast westward flows that appear during magnetically disturbed times and typically in the evening sector. Initially termed "polarization jets" by Galperin and Zosimova (1974), they were later referred to as SAID by Spiro et al. (1979) and included in the generic term "Sub Auroral Polarization Stream" (SAPS) by Foster and Burke (2002), Mishin (2013) and Mishin et al. (2017) later argued that SAPS implied a different generation process when compared to an SAID. The generation of SAID channels was first explained by Southwood and Wolf (1978) as sourced from a voltage generator, and later by Anderson et al. (1993) as sourced from a current generator, with the closing ionospheric currents being the main driver. Both theoretical (De Keyser, 1999) and observations from ground-based and space-based sensors (Anderson et al., 1991, 2001; Archer & Knudsen, 2018; Foster et al., 1994; Puhl-Quinn et al., 2007) have shown that SAID channels are characterized by elevated electron and ion temperature and a depletion in the electron density known as a trough. The low electrical conductivity in the trough plays an important role in the development of the large flow velocities that characterize SAIDs (Zheng et al., 2008).

Recent studies suggest that SAID channels are associated with the Strong Thermal Emission Velocity Enhancement (STEVE) aurora. STEVE, a new type of aurora discovered initially by citizen scientists (MacDonald et al., 2018), is distinct from the classical auroras. It is characterized by a narrow ribbon of light appearing at subauroral latitudes, often associated with a "picket fence" of green vertical stripes. STEVE has generated considerable interest among scientists and the public due to its distinctive appearance and unusual behavior (Archer, Gallardo-Lacourt, et al., 2019; Archer, St.-Maurice, et al., 2019; Gallardo-Lacourt, Liang, et al., 2018; Gallardo-Lacourt, Nishimura, et al., 2018; Nishimura, Donovan, et al., 2020; Semeter et al., 2020), with particular interest in its optical spectra (Gillies et al., 2019; Liang et al., 2019; Martinis et al., 2022) and magnetosphere

connections (Nishimura, Yang, et al., 2020; Nishimura et al., 2019). Despite its striking appearance, the physical mechanisms behind the STEVE origin and emissions remain largely unresolved.

One pathway that tries to explain the generation of STEVE is explained as an evolution of a Stable Auroral Red (SAR) (Gillies et al., 2023). A for the emissions, it's continuum spectrum could be caused by [N_2] vibrational excitation (Harding et al., 2020). The work of Mishin and Streltsov (2019), Mishin and Streltsov (2022, 2023, 2024) shows the essential role of the vibrational excitation of [N_2] in the STEVE spectrum and the importance of the depleted density profile in the SAID channel. Their results explain the intense SAID found in the Swarm/STEVE data set, the STEVE and picket fence optical spectra, and the basic features of the SAR-arc-into-STEVE transition reported by Gillies et al. (2023) and Martinis et al. (2022). This is not the only pathway, as STEVE related SAID have been observed without a precursor SAR arc (Nishimura et al., 2023). While classic auroras are caused by collisions between precipitating charged particles and atmospheric atoms and molecules, the processes giving rise to the distinct features of STEVE are still unclear. Sparse measurements available indicate that the flow channel associated with STEVE shows velocities larger than 5 km/s and an electron temperature higher than 10,000 K at Low Earth Orbit (LEO) altitudes, suggesting it could be an extreme version of an SAID flow channel (Archer, Gallardo-Lacourt, et al., 2019; Archer, St.-Maurice, et al., 2019).

The study of STEVE and extreme SAIDS faces a greater challenge when the observations exceed the designed measurement range of the sensor, leading to a disconnect between theory and measurements. While 2D studies have attempted to simulate such channels (Liang et al., 2021, 2022), we include a full 3D approach capable of resolving what we find to be substantial longitudinal variations and dynamics in the flow channels. Lynch et al. (2022) showed in 3D how FAC tearing mode are a plausible explanation for the picket fence visible signature.

The transient and relatively rare nature of STEVE presents a challenge for experimental measurement. Modeling has emerged as a powerful tool for investigating the behavior of the ionosphere and its interactions with the Sun, the Earth's magnetic field, and the lower atmosphere, including STEVE. Various modeling techniques are available, ranging from empirical methods to complex physics-based numerical simulations. Empirical methods, such as IRI (Bilitza et al., 2022), NRLMSIS (Emmert et al., 2021), and NEQuick (Radicella, 2009), are based on mathematical functions derived from historical experimental data. However, such empirical models may not be able to simulate conditions in the ionosphere when STEVE is present. On the other hand, physics-based models such as TIEGCM (Qian et al., 2014), GITM (Ridley et al., 2006), and SAMI3 (Huba et al., 2008) are global models with a large grid size and geographical coverage, making it difficult to simulate STEVE due to its narrow nature. The GEMINI ionospheric model (Zettergren & Semeter, 2012) can address this issue by incorporating inputs from empirical models and allowing for a grid size that can be adjusted to cover a smaller geographical area than global models. Designed for medium to small spatial scales (200 m–10,000 km), GEMINI is well-suited for simulating extreme SAID flow channels.

GEMINI (Zettergren & Snively, 2019) is used in the current study to simulate an extreme SAID event using a 3D grid, using inputs motivated by existing experimental measurements. It is notable, however, that the extreme temperatures and flows within STEVE create a significant gap between observations and theory/modeling and, indeed, create some additional challenges with various parameters used in physics-based models. While relatively sparse extreme SAID observation still serve as a valuable starting point for the modeling process. GEMINI is driven by a constant current density shaped by previous STEVE measurements (Nishimura, Donovan, et al., 2020). The E-region is of particular interest as there are no direct measurements that can elucidate the processes dominating the ionosphere in these extreme cases.

Our results show flows and current from an extreme SAID channel and how these exceed existing current measurements of STEVE. The simulations have revealed complex structures and behaviors, emphasizing the importance of 3D simulations in capturing these phenomena. The interplay between plasma depletion, conductance increase, and channel velocity increase is confirmed, even in the extreme values of 12 km/s. The study has also highlighted the role of various factors, such as current density and longitudinal length, in influencing the behavior of the channel velocity. However, these simulations should be viewed as approximations due to the limited experimental observations available to constrain the model inputs and the assumptions made to achieve sensible results. We are exploring behaviors at the limits of current simulations, with values that escape the existing formula and models for ionospheric parameters and whether these effects occur physically is not known.

The paper is structured as follows: Section 2 details the model setup, describing the ionospheric conditions used as inputs to the model and the modifications made to accurately simulate the behavior of an extreme SAID channel. The results of a 3D simulation obtained from GEMINI are presented in Section 3. Section 4 explores these results and their implications, comparing them to a 2D simulation also conducted with GEMINI. We conclude with a summary of all results and the future work ahead in Section 5.

2. Model Setup

The **G**eospace **E**nvironment **M**odel of **I**on-**N**eutral **I**nteractions (GEMINI) (Zettergren & Semeter, 2012; Zettergren & Snively, 2019) is a versatile three-dimensional ionospheric model, specifically designed to capture a wide range of phenomena occurring at medium to small spatial scales (200 m–10,000 km). GEMINI is designed to function in either two or three dimensions, utilizing general orthogonal curvilinear coordinates, typically a tilted dipole (Huba et al., 2000) or a Cartesian system. The model employs a fluid system of equations (Blelly & Schunk, 1993; Schunk, 1977) to describe the dynamic behavior of the ionospheric plasma, which is self-consistently coupled to an electrostatic treatment of auroral and neutral dynamo currents. The fluid system includes three conservation equations (mass, momentum, and energy) for each ionospheric species s relevant to the E-, F-, and topside E-regions ($s = O^+, NO^+, N_2^+, O_2^+, N^+, H^+$).

To accurately model an SAID channel under extreme conditions, GEMINI must be configured appropriately. Some initial conditions, such as magnetic declination and neutral compositions (determined by MSIS00), are already handled by the model for a given location. However, users input additional configuration parameters, including drivers and grid size. To drive the SAID channel in the model a user-specified current density must be used. For our case we use the measurements from the Defense Meteorological Satellite Program (DMSP) presented in Nishimura, Donovan, et al. (2020) and Nishimura, Yang, et al. (2020) as an initial reference. These DMSP measurements represent some of the best constraints available for the field-aligned currents of the STEVE/SAID channel, which should aid in accurately simulating the channel dynamics.

From Nishimura, Donovan, et al. (2020), the DMSP measurements show a flow channel velocity with a maximum velocity of 4.5 km/s and temperatures reaching approximately 4,500 K. These measurements appear to be saturated by the maximum values the sensor can measure. Therefore, they will be used cautiously and as a reference, with our objective being to model plasma flows larger than 5 km/s and temperatures hotter than 5,000 K. Field-aligned current density (FAC) values go as high as 1 $\mu A/m^2$, which will be our upper boundary target for the current density that the system will be driven with. There also exists a detached precipitation on the upward portion of the field-aligned current. Following the results of Liang et al. (2022), a precipitation profile was used on the upward portion of the current density with a maximum value of 0.5 mW/m^2, modeling a current that is partially carried by precipitating electrons.

GEMINI assumes fixed potential at the lateral boundaries of the grid (Dirichlet boundary conditions), while the FAC at the top of the model is effectively treated as a source term for the field-integrated potential equation (Zettergren et al., 2015). For the fluid system of equation, at the bottom boundary, conditions are taken such that $T_s = T_n$, and at the top boundary, $T_s = T_\infty$, where T_∞ is defined in the input file to the model. However, for our particular case, we are interested in analyzing the effect of the current and the channel on the ionosphere. Thus, the top boundary condition was modified to allow energy to move freely across it by setting a specified heat flux instead of T_∞, that is, the energy equation solution was changed to incorporation Neumann conditions for electron heat conduction. In our simulations, the heat flux was set to zero, so that energy can stay in the ionosphere rather than a massive amount of heat escape at the top. Table 1 provides an overview of the most important input parameters for the model.

GEMINI simulations are conducted in two steps: an initialization/equilibration phase and a "disturbance" simulation. The primary objective of the initialization phase is to establish equilibrium within the ionospheric parameters. This involves running the model for a sufficient duration, typically several hours to a day in simulation time. The resulting equilibrium offers a snapshot of ionospheric conditions as the grid undergoes slow diurnal variations in energy inputs.

In the simulations conducted for the current study, GEMINI outputs are organized along three internal coordinates: the x_1 coordinate aligns with the magnetic field line, x_2 increases as the L-shell number grows, approximately in a northern direction, and finally, x_3 is the zonal direction (positive east). Output data in the

Table 1
Basic Parameters Used to Run GEMINI

Parameter	Value
Duration of sim	900 s
Output interval	1 s
Grid size	512 × 512 × 512 (lphi,lp,lq)
Model Latitude span	58°–63° North
Model Longitude span	55°–125° East
Altitude span	0–1,000 km
Current density target	0.6 μA/m^2
MLT at the center longitude	21

model native coordinate system is gridded onto a regular latitude, longitude, and altitude mesh for ease of visualization and analysis, allowing for a comprehensive representation of the spatial distribution of the simulated parameters. In this work we specifically use magnetic latitude and longitude for our plots.

2.1. Current Density and Precipitation Topology

To emulate the latitudinal changes in current density as shown by Nishimura, Donovan, et al. (2020) and Nishimura, Yang, et al. (2020), Gaussian functions of opposite sign with a small difference in their mean and maximum values were employed. Equation 1 presents the analytical expression of the latitudinal geometry of the current density, where lat represents the magnetic latitude. In this case, σ_{lat}, which represents the disturbance width, was chosen to be 0.02, which translates to a current density channel width at mid height of 0.5° in latitude. This approach ensures that the model accurately captures the dynamics of the SAID channel. Figure 1(top) shows how the shape of the current density applied. Black solid lines represents the function displayed in Equation 1, while the orange circles represent the actual GEMINI input as sampled by the grid.

$$J_{lat}(lat) = \exp\left(-\frac{(\text{lat} - \langle\text{lat}\rangle + 1.5\sigma_{lat})^2}{2\sigma_{lat}^2}\right) - \exp\left(-\frac{(\text{lat} - \langle\text{lat}\rangle - 1.5\sigma_{lat})^2}{2\sigma_{lat}^2}\right) \quad (1)$$

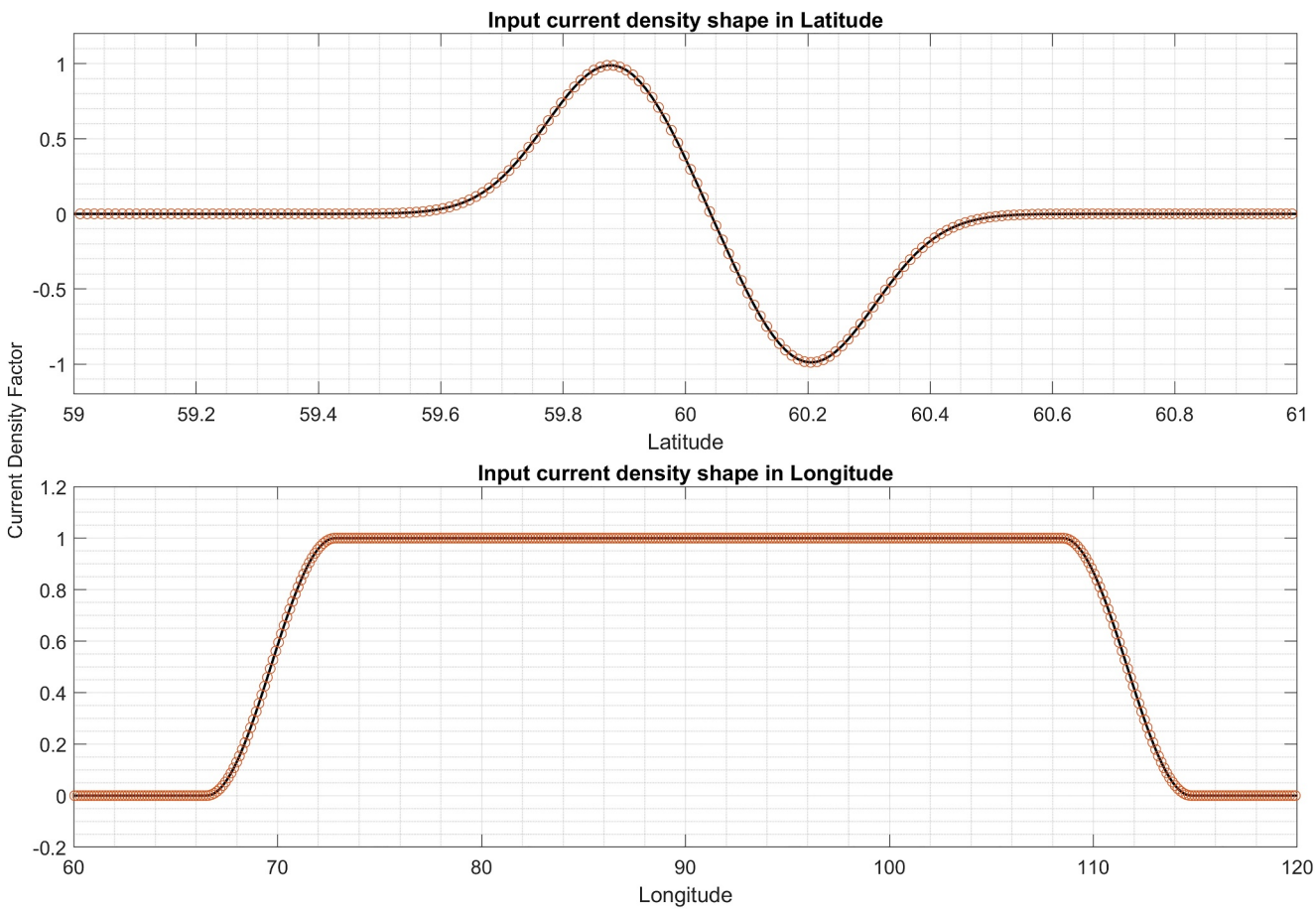

Figure 1. Riased cosine input current defined at the top layer of the grid.

Meanwhile, in the longitudinal case, a different approach was taken to generate a current density that remains constant for several kilometers before tapering to zero before reaching the boundaries of the simulation. This was accomplished by using a Raised Cosine window, with an analytical expression shown in Equation 2.

$$J_{lon}(lon) = \begin{cases} 1 & : |lon| \leq \dfrac{1-\beta}{2T} \\ \dfrac{1}{2}\left[1 + \cos\left(\dfrac{\pi T}{\beta}\left[|lon| - \dfrac{1-\beta}{2T}\right]\right)\right] & : \dfrac{1-\beta}{2T} < |lon| \leq \dfrac{1+\beta}{2T} \\ 0 & : otherwise \end{cases} \quad (2)$$

The Raised Cosine window facilitates the generation of a smooth curve with controllable characteristics. The shape of the window is determined by a parameter, denoted as β (roll factor), where $\beta = 1$ yields a pure cosine, while $\beta = 0$ results in a square window. In our case, we aimed to generate a current density profile that peaks in the center and gradually decreases toward the edges of the simulation domain in the longitudinal direction. To achieve this, we used $\beta = 0.15$ and a period of $T = 1/42$, which corresponds to a longitudinal extent of approximately 40° from midpoint to midpoint (2,200 km). The general shape is displayed in Figure 1(bottom), with the solid black line representing the shape of Equation 2 and the orange circles representing the actual GEMINI input as sampled by the grid.

As previously stated, electron precipitation was incorporated into the model. The precipitation profile mirrors the shape of the current density in the longitudinal coordinate and only includes the negative Gaussian for the shape in latitude. Both the central energy and total energy flux adopt this Gaussian shape, peaking at 0.5 mW/m^2 for the total energy flux and 2 KeV for the central energy. These values were chosen following the results of Liang et al. (2022), which included this precipitation in the upward part of the current, which also shows that this can be observed in DMSP measurements (Figure 7 of Nishimura, Donovan, et al. (2020)) or be inferred from the existing electron flux spectrograms (Mishin et al., 2017; Puhl-Quinn et al., 2007).

Our approach takes inspiration from previous works, particularly Liang et al. (2022), while it differentiates itself from these studies by including the longitudinal dimension on the simulations based on the observations of Nishimura, Donovan, et al. (2020) and Gallardo-Lacourt, Nishimura, et al. (2018). On the other hand, Lynch et al. (2022) applies an electric field driver, which produces a flow-induced conductance gradient, wherein the FACs adjust independently to create a self-consistent system, showing that the resulting current sheets may be tearing-mode unstable. By contrast, we are applying a current density driver, and allowing electric fields to adjust self-consistently. This adjustment involves a complex interplay between electric fields, flow velocities, ion chemistry, plasma depletion, and plasma temperatures. We expect the time-dependent development of the channel pushes key parameters up to and beyond their range of applicability and, indeed, limitations in the physical descriptions used in GEMINI. Our use of a current density driver could be argued as more realistic than an electric field driver, since the stored energy in the magnetosphere is expected to be inductive in nature, although both approaches have assumptions and limitations. Ultimately what might be needed is an Alfvenic boundary condition inside GEMINI, as discussed in Wright and Russell (2014). At the same time we will focus on the chemical processes in the E-region, something not shown by Lynch et al. (2022).

2.2. Changes to GEMINI Required to Accommodate Extreme Conditions

Since we simulate an extreme SAID channel, where velocities are expected to exceed 5 km/s, several adjustments must be made to the model to accommodate the anticipated extreme temperatures (above 30,000 K). Most of these adjustments are directly related to results obtained from laboratory experiments or other data, which are often fitted to relatively simple functional forms that can produce nonsensical results (e.g., negative collision frequency) when applied outside their domain of applicability. In the course of conducting the simulations for this study we found a number of such parameterizations that apparently break down for extreme ion or electron temperature values.

GEMINI values for electron-neutral momentum transfer collision frequencies were sourced from Schunk and Nagy (2009), who directly references Itikawa (1974). The latter obtained the momentum transfer cross-section for electron collisions from laboratory experiments and theoretical data. It is possible to use more recent results to

calculate the [N_2] cross-section by averaging the Majeed and Strickland (1997) and Itikawa (2006) cross sections over the electron distribution. However, averaging must take into account the effect of vibrational losses on the distribution functions, which depends on the $N_e/[N_2]$ ratio, which changes with altitude. This is expected to be added to GEMINI in the near future.

For simulation of extreme conditions the electron-N_2 collision frequency (Equation 3) and the electron-H collision frequency (Equation 4) pose a challenge since they are not positive-definite for arbitrary values of temperature (i.e., T_e).

$$\nu_{e-N_2} = 2.33 \times 10^{-11} n(N_2)\left(1 - 1.21 \times 10^{-4} T_e\right) T_e \tag{3}$$

$$\nu_{e-H} = 4.5 \times 10^{-9} n(H)\left(1 - 1.35 \times 10^{-4} T_e\right) T_e^{1/2} \tag{4}$$

In this work, to prevent negative collision frequencies, the electron temperature is capped at a value 1,000 K lower than the temperature at which the collision frequency crosses zero at approximately 7,000 for the electron-N_2 collision frequency and 8,000 for the electron-H collision frequency. This is done only for purposes of computing problematic quantities and allows the electron temperature to rise above that value, but a maximum fixed value is used in the calculations of the electron neutral collision frequencies. Ion-neutral collision frequencies do not face the same issue as their functional form is $\left(A - B\log_{10}\left(\frac{T_i + T_e}{2}\right)\right)^2$. Given this characteristic, no modifications were needed for ion-neutral collision frequencies.

Since the collision frequencies between electrons and some neutrals are affected, electron thermal conduction, which governs electron heat flow, is also impacted. Equation 5 shows the thermal conductivity directly taken from Schunk and Nagy (2009), which, in turn, references Banks (1966). Since this equation depends on the average of the momentum transfer cross-section $\left(\langle Q_{en}^{(1)} \rangle\right)$ between electrons and neutrals, it faces similar issues mentioned with electron-neutral collision frequencies. The electron-N_2 cross-section is given by $Q_{eN_2}^{(1)} = 2.82 \times 10^{-17}\left(1 - 1.21 \times 10^{-4} T_e\right) T_e^{1/2}$. Therefore, inside the electron thermal conductivity calculation these cross sections are also capped in the same fashion—at a temperature below the point where the function crosses zeron.

$$\lambda_e = \frac{7.7 \times 10^5 T_e^{5/2}}{1 + 3.22 \times 10^4 \frac{T_e^2}{n_e} \sum_n n_n \langle Q_{en}^{(1)} \rangle} \tag{5}$$

Another set of calculations that became problematic in our simulations at large temperatures is electron energy losses due to vibrational excitation of [N_2] and [O_2]. As described by Pavlov (1998), the [N_2] rotational losses have a rather complicated analytical expression which is only valid for values of electron temperature between 3,00 and 6,000 K. Similarly, Jones et al. (2003) results show how the [O_2] vibrational losses are only valid for values of electron temperature between 300 and 6,000 K. One might be tempted to utilize these functions above 6,000 K, but since these two vibrational losses are logarithms of polynomial fittings, their behavior outside of the range of 6,000 K is of an unbound growth. As such, all electron temperatures were capped at 6,000 K when calculating vibrational losses. Additionally vibrational rates in the 300–6,000 K range were updated to include the most recent work on these topics (Schunk & Nagy, 2009).

GEMINI also required some changes to the numerical solvers to obtain stable results at extremely large flows and temperatures. Normally GEMINI will resolve the temperature equation as a series of operator splits that individually resolve substeps of (a) advection, (b) compression, (c) thermal conductivity, and (d) source-loss terms. We have found that these different terms are best resolved in order of increasing numerical stiffness—in normal conditions for the ionosphere in the order listed above. However, at very high temperatures the thermal conduction and complicated source-loss process essentially compete for control of the temperature. In this case we have found that artificial oscillations in time can result unless one resolves numerical substeps c and d *simultaneously* so they may balance each other instantaneously in the code. Thus, we have found it necessary in our simulations to solve both thermal conduction and energy source loss terms together in a single substep. For this study, we use either a TRBDF2 (LeVeque, 2007) or backward Euler numerical solutions for the resulting diffusion-reaction type equation. This is in contrast with the standard GEMINI approach of resolving a diffusion

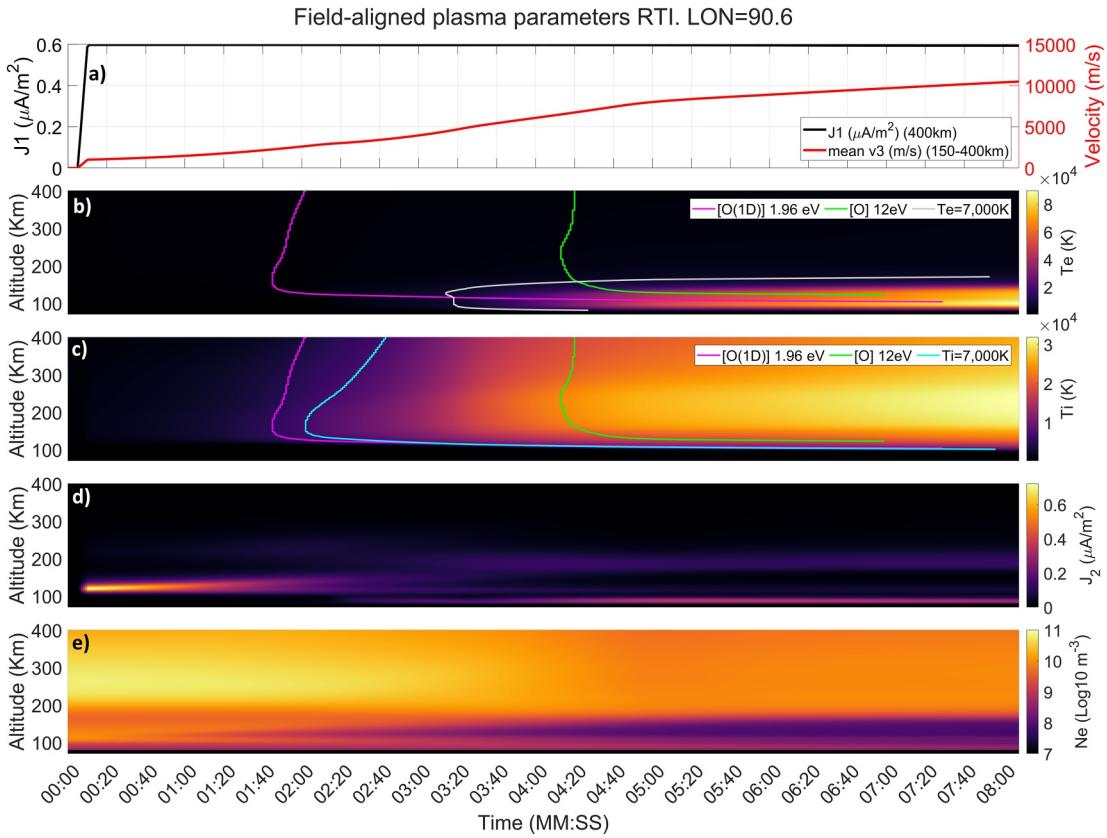

Figure 2. Field-aligned profiles are taken at the center of the flow channel. Panel (a) displays values for parallel-to-B current density (J_1) and east/west velocity (v_3) averaged from 150 to 400 km. Panels (b) and (c) show electron (T_e) and ion (T_i) temperatures. Panel (d) depicts the north/south current (J_2), while panel (e) provides insights into the total electron density (N_e).

equation with TRBDF2 and feeding the result into a reaction equation that uses an exponential time differencing scheme (a split operator approach).

3. Simulation Results for an Extreme SAID Channel

3.1. 3D Simulation

In this section, we present the results of our 3D simulations of an extreme SAID. We focus only on a portion of the simulation outputs, with the a complete set of outputs (N_s, v_{1-3}, T_s, J_{1-3}, E_{2-3}, σ_P, σ_H) available as Figures and Movies in the supporting material (Figures S1–S19 in Supporting Information S1, Movies S1–S17). Our main focus will be on the spatial and temporal variations of the plasma density ([Ne], $[NO^+]$, $[O^+]$, and $\left[O_2^+\right]$), ion and electron temperature (T_i and T_e), closure current (J_2), and channel velocity (v_3), which are key parameters to characterize the SAID phenomenon.

Figure 2 displays simulation results, focusing on field-aligned profiles at the flow channel center in both latitude and longitude. It particularly highlights the channel velocity, the driving and closure current, as well as the ion and electron temperature. The center in latitude is defined as the location of zero FAC between the upward and downward current density (J_1), where temperatures and densities undergo the most drastic changes. The center in longitude is defined as 90°.

The extra lines included in panels (a) through (e) represent points in time and altitude where a model parameter surpasses a certain threshold where physics not included in the model could start taking effect. The magenta represents the point where the total energy (kinetic + thermal) of $\left[O_2^+\right]$ reaches the energy needed to trigger the first exited state of $[O]$, O(^{1}D), at 1.96 eV. The green line on the other hand is the point where the total energy of $\left[O_2^+\right]$ reaches the energy needed to ionize $[O]$, at 12 eV, with $[NO^+]$ reaching the same threshold just a second or

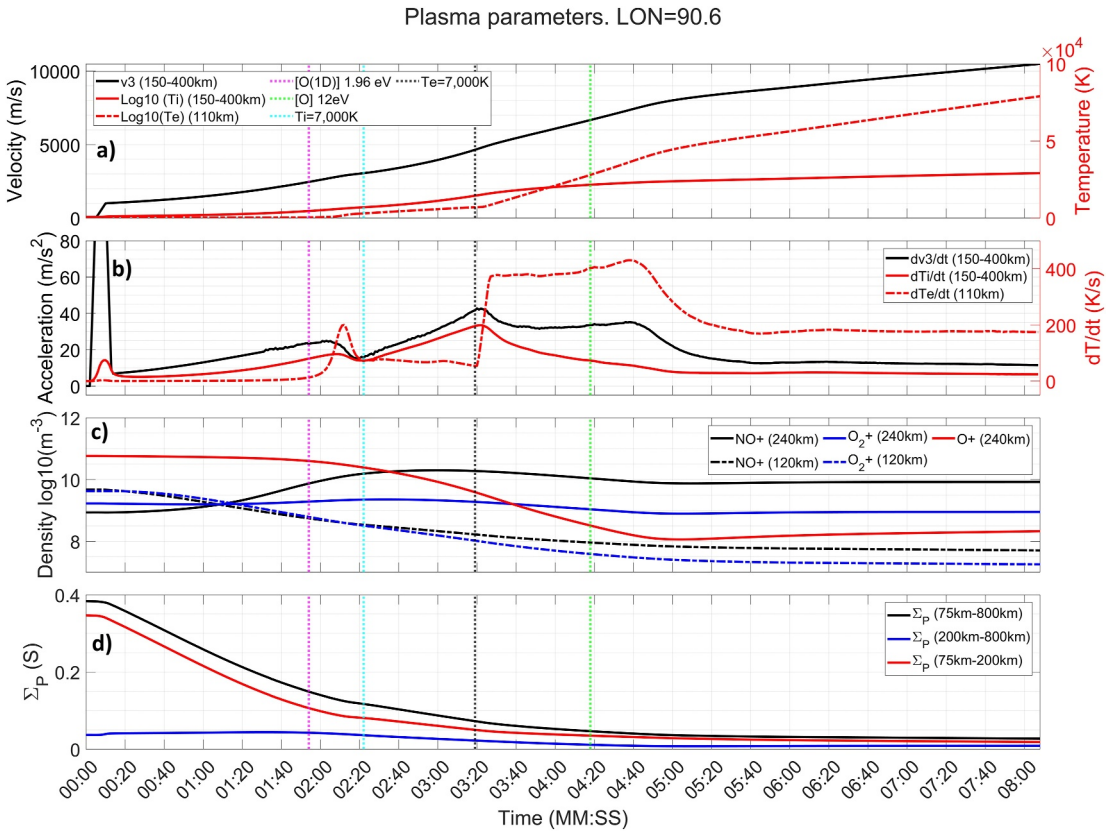

Figure 3. Key simulation output parameters. Panel (a) shows the average channel velocity (v_3, solid black line) and ion temperature (T_i, solid red line) between 150 and 400 km, as well as the electron temperature (T_e, dashed red line) at 110 km. Panel (b) shows the time derivative of all variables shown on panel (a). Panel (c) shows the density of the main ions, $[NO^+]$ and $\left[O_2^+\right]$ at 120 km (black and blue solid lines) and 240 km (black and blue dashed lines) as well as $[O^+]$ at 240 km (solid red line). Panel (d) shows the total height integrated Pedersen conductance (Σ_p, solid black line), as well as the F-region (200–800 km, solid blue line) and E-region (95–200 km, solid red line) contribution.

two after due to is marginally smaller atomic mass. Finally, the cyan and gray lines represent the points in time and altitude where the ion and electron temperature reach 7,000 K, respectively. 7,000 K is an important temperature, since many equations are only valid until that point, even if they do not cause the model to break due to unexpected negative values. For the ion temperature this only applied currently to the losses due to the vibrations and rotational modes of $[N_2]$ and $[O_2]$. Most ion-neutral collision frequencies are also defined up to this threshold, but since their depends is mostly Log10 with temperature, extending to larger temperatures does not cause large issues. For the electron case, it is the point where some electron-neutral collision frequencies are capped as explained in Section 2.2, as well as marking the top boundary where other uncapped electron-collision frequencies are valid. This will be important further on, since for large temperature these electron-neutral collision will grow linearly with temperature. Figures S1, S6, S11, and S16 in Supporting Information S1 show these thresholds and the energy of $\left[O_2^+\right]$ for further analysis.

Figure 3 serves as a companion to Figure 2, focusing specifically on channel velocity, temperatures, specific ion densities, growth rates in velocity and temperature, as well as height-integrated conductivity. Analogue to Figure 2, the magenta, green, and cyan lines represent the same thresholds mentioned above, with the black line replacing the gray one for better visibility.

In the initial 5 s of the simulation, no current driver is applied. J_1 grows linearly over the next 5 s to a value of approximately 0.6 μA/m^2 at an altitude of 400 km, and remains constant for the rest of the simulation, as shown in panel (a) of Figure 2. During this brief time frame, the channel velocity increases to 1 km/s at 00:10. A shorter growth time for the driving current was chosen to isolate the effects of a large current driving the extreme channel. The east/west velocity of the channel (v_3) is also displayed in Figure 2a, revealing a changing slope. The

distinctions between different time phases become more apparent in Figure 3, from which we can identify four different phases.

The first phase, from 00:10 to approximately 02:10, there is an exponential increase in the channel velocity v_3, starting from 1 km/s and ending with 2.8 km/s at the 02:10 mark. This increase is accompanied by a growth in both electron and ion temperatures, with the ion temperature remaining below 6,000 K and the electron temperature below 2,000 K, as depicted in Figure 3a. The growth in ion temperature coincides with the growth in channel velocity, as they are related, as explained by St-Maurice et al. (1999).

Two important thresholds are reached by the end of this section. First, the ion temperature is now high enough for the reaction $[O^+] + [N_2] \rightarrow [NO^+] + [N]$ to accelerate as the temperature increases. This implies that most of the $[O^+]$ in the lower F-region will be converted to $[NO^+]$ (St-Maurice & Laneville, 1998). Second, $\left[O_2^+\right]$ has enough energy to trigger inelastic collisions that excite $O(^1D)$. Therefore the two main ions in the E- and lower F-region will start to lose some of their energy to this inelastic process that is not included in GEMINI, reducing the channel velocity without affecting the electric field. This will affect plasma from 110 km and above. Inelastic collisions can be considered the first factor not included in GEMINI that will stop the growth of the channel velocity.

The primary closing current (J_2) occurs between 110 and 130 km, as seen in Figure 2d. On the other hand, the density, as shown in Figure 2e, is gradually starting to deplete, with the first signs appearing around the 00:30 s mark.

The depletion of plasma in the E-region, where most of the current is closing, leads to a decrease in the Pedersen conductivity. To maintain a constant driving current, this, in turn, necessitates an increase in the poleward electric field within the channel, meaning an increase in the channel velocity. The layer of the closure current J_2, as depicted in Figure 2d, also spreads to a higher altitude due to the loss of the E-region density. When we compare this information with Figure 3b, we observe that the first phase concludes approximately when the acceleration reaches a local maximum. The local minima achieved right after the end of the phase coincides with point where the ion temperature reaches 7,000 K, the threshold marked by the cyan line.

Figure 3c displays the densities of the main ion species ($[NO^+]$ solid black line, $\left[O_2^+\right]$ solid blue line, and $[O^+]$ solid red line). We note that the first phase is characterized by a continuous growth of $[NO^+]$ and a subsequent decrease of $[O^+]$ at 240 km, which is expected since the ion temperature is sufficiently high for that reaction to occur. Concurrently, the densities at 120 km are steadily decreasing (black and blue dashed lines). The local maximum appears to align itself to a point where $[NO^+]$ and $[O^+]$ are comparable. Finally, Figure 3d illustrates how the total Pedersen conductance (solid black line) rapidly decreases during this first phase, becoming 33% of its original value by the 02:10 min mark. Most of this change is attributed to the E-region conductance (solid red line) as the plasma gradually depletes in the area.

The second phase occurs between the two local maxima (02:10 and 03:20), as depicted in Figure 3b, where abrupt changes to the acceleration occur, reaching a maximum of 42 m/s^2 by the end of the phase, with a final channel velocity of 4.8 km/s. During this same period, the electron temperature remains below 7,000 K, while the ion temperature rises to 15,000 K. Even though the electron temperature has not reached the point where it goes beyond 7,000 K, there is a particular phenomena happening between 02:03 and 02:20 where there is a sudden change to the electron temperature, jumping from approximately 700 K all the way to 3,000 K it a span of 17 s. This change is also visible in the growth rate of electron temperature. The reason for this is frictional heating due to the large electric field, that reaches a value of 200 mV/m at the 02:10 min mark. From the Supporting Movie S3 it is possible to see how this enhancement goes from 150 to 100 km. Due to the enhanced electric field, the frictional heating at these altitudes is now considerable and thus triggers this enhancement of electron temperature.

The most significant changes are observed with the closing current and the total plasma density, as shown in Figures 2d and 2e, with the current dividing into several smaller channels as the density in the E-region becomes entirely depleted. The end of the phase coincides with the point where the electron temperature reaches 7,000 K, and so our electron-neutral collision frequencies from now on are outside of the bounds of their respective equations.

This can be considered a transition phase in terms of closure current, with a small amount of current still flowing through the E-region. However, since the plasma in that area is constantly being depleted, some current is now

flowing through the lower F-region and at an altitude of 100 km. The increase in electron temperature to such high values is directly attributed to the frictional heating term in the energy equation for the electrons ($Q_e = m_e \nu_e n_0 E^2 / B^2$). This enhanced electron temperature extends down to 85 km and causes the electron-neutral collision frequency to rise to a value comparable to the local electron cyclotron, thus enabling electrons to carry a Pedersen current at an altitude of 100 km. The inelastic collision that should have trigger on the previous phase will also have the effect of decreasing the frictional heating by soaking up energy out of the plasma. This also explains why the phase ends with a decrease in acceleration as well as a slower decrease in the Pedersen conductance, since there is some small conductivity being generated by these collisional electrons.

Figure 3c illustrates how the density at 240 km of $[O^+]$ rapidly decreases during this period. On the other hand $[NO^+]$ slows its increase, reaching a maximum of $2 \times 10^{10} \mathrm{m}^{-3}$. This can be attributed to the recombination of $[O^+]$, which becomes almost completely depleted, preventing the reaction from occurring at a higher rate. The boundaries of this phase also align with the points where $[O^+]$ becomes comparable to $[NO^+]$ at the beginning, and where it becomes comparable (within an order of magnitude) to $[O_2^+]$ at the end. At 120 km, we observe the densities rapidly decreasing at an exponential rate. The total conductance in Figure 3d steadily decreases just as before, with the E-region once again being the main contributor to this decrease, although the F-region does see some decrease. As such, the rapid increase in acceleration and temperature can be readily explained by the plasma being primarily depleted in the E-region, with a minor contribution from the F-region. Since this section ends with the point in time where the electrons reach 7,000 K, the electron-neutral collision frequencies are still valid during this period.

The third phase exists between the second set of local maxima, starting at 03:20 and ending at 04:40. It is possible to see how right after the end of the second phase, which coincides with the point where the electron temperatures reaches 7,000 K, there is an explosive growth of the electron temperature and an intensification of the current density at 100 km. This happens because a decision was made not to cap the temperature when calculating the collision frequencies unless absolutely necessary, since one of our objectives is to show and make evident that the collision frequencies commonly used in SAID modeling are not valid under the extreme conditions of SAID-STEVE events. These collision frequencies applied in our simulations can grow unbounded, causing the electron frictional heating term to grow in the same manner. The positive feedback of a large and growing electric field and the collision frequencies depending on the temperature itself causes the frictional heating between 100 and 150 km to skyrocket, particularly caused by the collisions between electrons and $[O_2]$.

This phase is where the maximum growth of the channel velocity occurs, starting at a velocity of 4.7 km/s and ending with 7.4 km/s as seen in Figure 2a. This period also shows significant increases in ion temperatures, though much more measured than the electrin temperature changes. From Figure 3b, we can see that the acceleration ends with a value of 40 $\mathrm{m/s}^2$, the ion temperature growth starts at a 200 K/s and only decreases as the phase progresses, and the electron temperature experiences the largest growth rate at 470 K/s. By the end of the phase, electrons at an altitude of 110 km have reached a temperature of 37,000 K, with the average ion temperature between 150 and 400 km reaching 23,000 K. The reaction between $[O^+]$ and $[N_2]$, which was extended to 70,000 K by Liang et al. (2021), is still valid during this phase.

Another milestone is reached during this phase, since $\left[O_2^+\right]$ reaches 12 eV at the 04:20 min mark. As seen on 2e), we see how there is a sizable portion of the E-region that will have ions with energies large enough to ionize the neutral $[O]$ in the atmosphere. As such, there will be an increase in plasma from 120 km up caused by impact ionization from this point on. This means that the conductance will start to increase during this time frame for the same altitude range, decreasing the need for such a large electric field and lowering the channel velocity. Impact ionization can be considered the second factor not included in GEMINI that will stop the growth of the channel velocity.

The two time limits of the phase also roughly coincide with two milestones in the plasma density as seen in Figure 3c. The 03:20 mark is where the density of $[O^+]$ at 240 km becomes comparable with the density of $\left[O_2^+\right]$, whereas the 04:40 mark is where $[O^+]$ reaches values comparable to the densities of $[NO^+]$ and $\left[O_2^+\right]$ in the E-region, at an altitude of 120 km. From Figure 3d, we see that the conductance has reached a value of 0.04 S, almost 10% of its original value of 0.38 S.

The final phase takes from 04:40 to 08:00. As depicted in Figure 2a, the channel velocity grows at a constant rate, with Figure 3b confirming an almost constant acceleration of 14 $\mathrm{m/s}^2$. The final velocity of the channel is

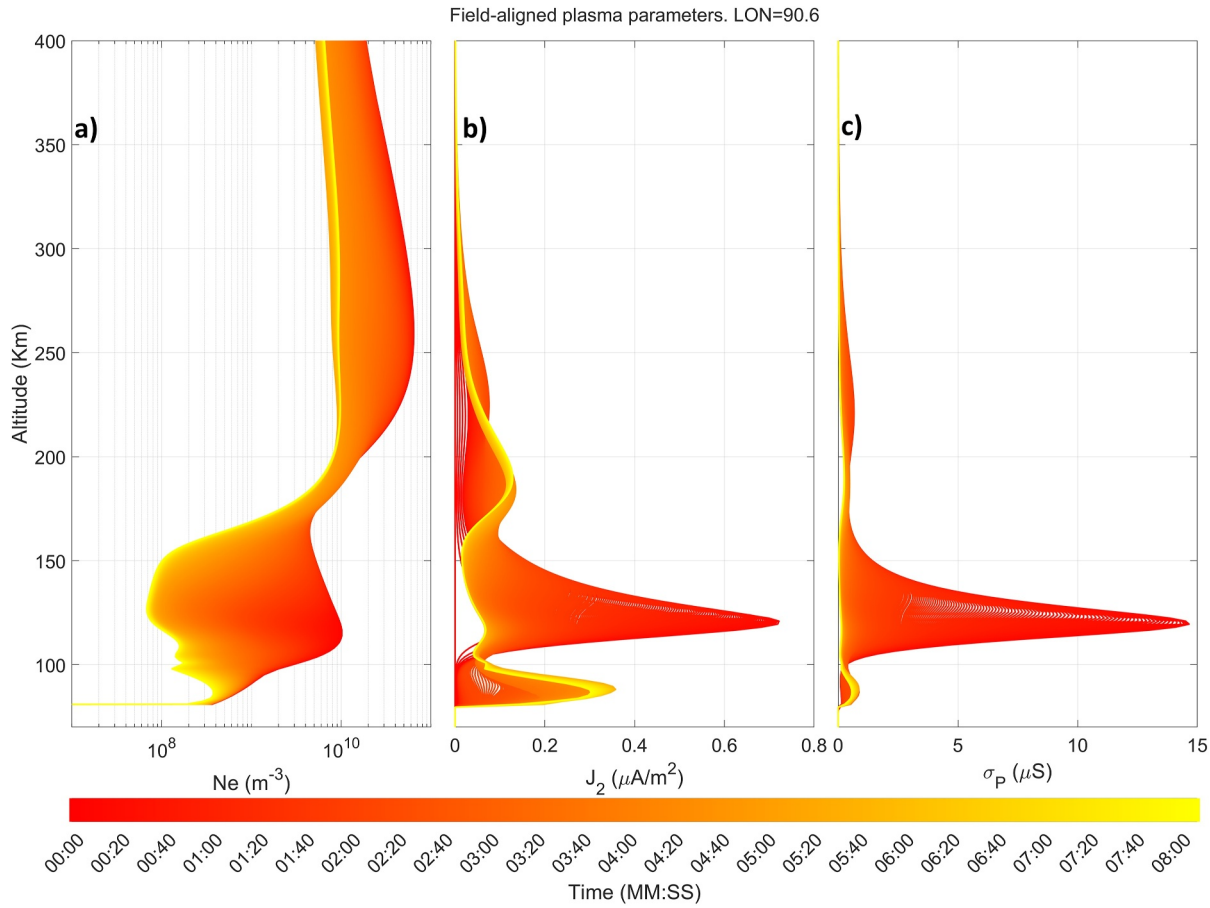

Figure 4. Field-aligned plasma parameters. Time is represented as a gradient from red to yellow as seen on the bottom bar. Panel (a) plasma density at the center of the channel. Panel (b) closure current density (J_2) at the center of the channel. Panel (c) Pedersen conductivity at the center of the channel.

approximately 10.5 km/s The ion and electron temperatures also increase linearly, as seen in Figures 2b and 2c, 3a and 3b. From Figure 2d, we observe that the current density in the 110–130 km altitude range is almost non-existent, with most of the current flowing either in a narrow band at 100 km or a wider band at 180 km. The plasma density in the E-region reaches values below 10^8 particles/m^3, as seen in Figures 2e and 3c. This final phase is characterized by a constant value of $[NO^+]$ and $\left[O_2^+\right]$ at 240 km, with a slight increase in the density of $[O^+]$. In the F-region, the plasma density is slowly decreasing. Finally, the conductance reaches a minimum value of 0.027 S, as seen in Figure 3d.

Figure 4 depicts the temporal changes in plasma density (panel a), closure current (panel b), and Pedersen conductivity (panel c) at the center of the flow channel. The progression of time is color-coded from red to yellow, as shown at the bottom of the figure. This display provides a better representation of the quantitative variations in parameters. Panel (a) reveals a continuous depletion of plasma density at all altitudes throughout the lifespan of the channel, particularly at 130 km. Here, the density decreases until it reaches a minimum of $7 \times 10^7 m^{-3}$, corresponding to an extremely low value of 70 particles/cm^3.

Figures 4b and 4c provide insight into how the changes in conductivity and closure current correspond to the behavior of the plasma density. Initially, most of the current flows at 120 km, decreasing rapidly as time progresses and the conductivity diminishes. Toward the end of the simulation, the conductivity is nearly 0 between 100 and 130 km, forcing the current to flow from 140 km upwards to 300 km, with a peak at 180 km. The existence of density and extreme temperatures below 100 km contribute to the conductivity in the area, which is why we see current flowing below 100 km. This current grows with time, but after reaching a maximum value of 0.34 μA/m^2, it starts decreasing, as does the plasma at that altitude.

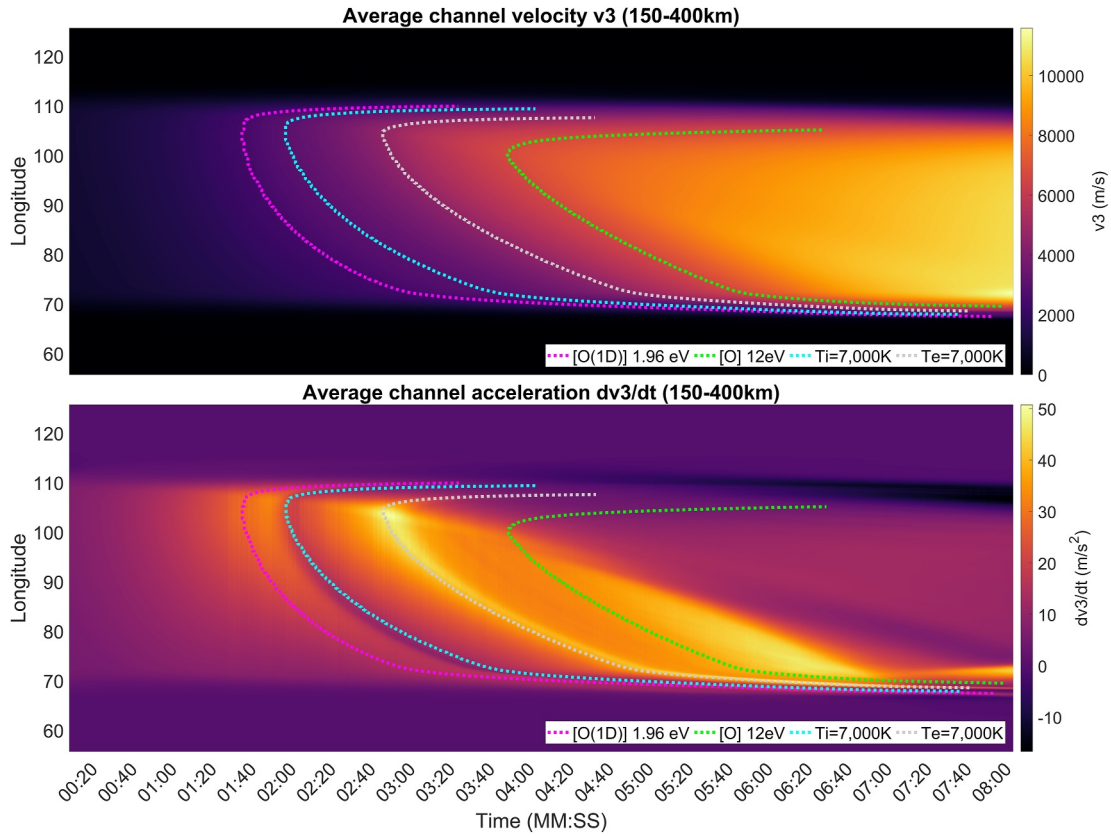

Figure 5. Average channel velocity (top panel) and acceleration (bottom panel) between 150 and 400 km. *Y* axis represents longitude at the center of the channel. Simulation starts when the 90° longitude point reaches 21 MLT. Threshold lines are also included.

The simulation spans over 40° in longitude, approximately 2,200 km, making it crucial to address the differences in longitude in the flow channel. Both Nishimura, Donovan, et al. (2020) and Gallardo-Lacourt, Nishimura, et al. (2018) set the length in longitude to be close to the value we utilize. Figure 5 displays both the average channel velocity from 150 to 400 km at the center of the channel and parallel to the magnetic field lines in the top panel, and the average channel acceleration between the same locations in the bottom panel. The *Y*-axis represents the longitude. Since the center of the channel is at 21 MLT, the larger the longitude, the further we are from the subsolar point.

Figure 5a illustrates how the channel velocity grows faster at larger longitudes from 00:20 to 03:00. This is an expected result, since due to the day/night cycle of GEMINI, the eastern side will have less plasma density due to recombination in the absence of the dayside photoionization; that is, this part of the channel has been in darkness longer than the western portion. The threshold for the energies and temperature previously defines also have the same behavior, starting first on the eastern side and later on toward the west. The cyan line, representing the point where the ion temperature reaches 7,000 K, coincides perfectly at all longitudes with the minimum value of channel acceleration, and thus close to the end of the first phased defined before.

From 03:00 to 06:00, the maximum channel velocity travels from the eastern side toward the western side, finishing with somewhat uniform channel velocity along longitudes, but with a peak in the far west. From panel (b), the acceleration shows us how the different phases that were mentioned before exist in longitude, with Figure 3 being a cut at the 90.6° in longitude. On the eastern side, there is a peak-valley-peak configuration, which differs from Figure 3 where there were three distinct peaks in the acceleration. The first peak-valley-peak configuration has this "travel" behavior, where it starts first on the eastern side and "travels" to the western side as time goes on. The first peak is also more pronounced toward the east and almost disappears toward the west. The second peak has a similar behavior, with it being more pronounced on the eastern side, though it remains constant in magnitude as we move closer to the west. Following the same east to west motion, we see how

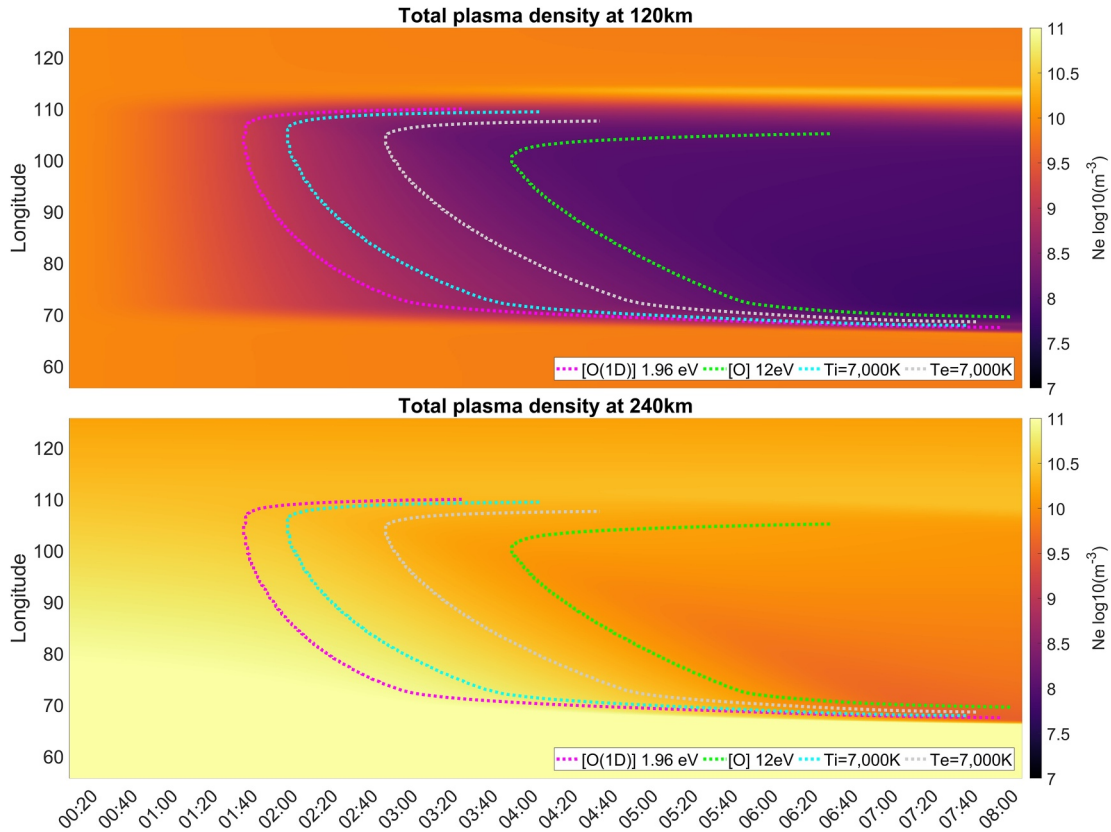

Figure 6. Total plasma density at 120 km (top) and 240 km (bottom). *Y* axis represents longitude at the center of the channel. Simulation starts when the 90° longitude point reaches 21 MLT.

the first peak and valley take longer to appear the westwards we are. Once again, we have a perfect alignment of this second high peak in acceleration with the point in time where the electron temperature reaches 7,000 k (gray line).

The third peak in acceleration starts to show up at approximately 95°, with it becoming more pronounced the further westward we go. By focusing on the changes in density at these two altitudes with longitude at the center of the channel, we can gain further insights. Figure 6(top) illustrates how the total plasma density at 120 km changes over time at the center of the channel in longitude, while Figure 6(bottom) shows the total plasma density at 240 km. It's evident that the density depletion at 120 km follows the same pattern as the average channel velocity as seen in Figure 5(top). The depletion is faster on the eastern side at the beginning, with the maximum depletion zone moving from east to west as time progresses. By the end of the simulation, the western side is slightly more depleted than the eastern side at 120 km, which directly correlates to the slightly larger velocity in the same area.

As for the density at 240 km, we observe that it takes much longer for depletion to occur, and the depletion is not as extreme as it is in the lower ionosphere. However, it still approaches a decrease of one order of magnitude in the western side by the end of the simulation. This also exhibits the same behavior in terms of where the depletion starts, being depleted first on the eastern side, while the west becomes much more depleted but later in time. This confirm that the final peak happens due to an marge larger depletion of plasma, since the western portion of the F-region sees a much larger depletion that its eastern counterpart.

Even though the F-region plasma density does not have a significant impact on the channel velocity when compared to the E-region plasma density, the gradient in F-region density from east to west contributes to the "travel" behavior of the average channel velocity. These results underscore the complex interplay between various factors in influencing the behavior of the channel velocity.

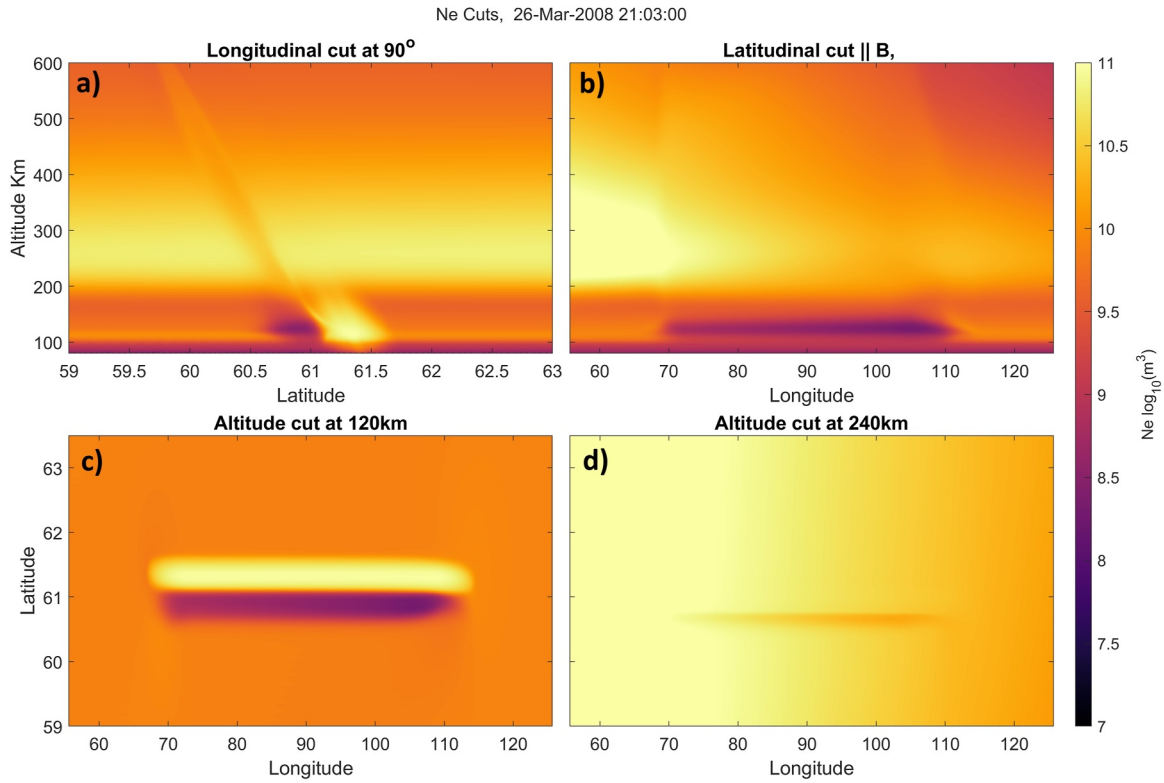

Figure 7. Plasma density at 03:00. Panels (a) is a cut in longitude at 90°. Panel (b) in cut in latitude along the magnetic field line. Panels (c) and (d) are altitude cuts at 120 and 240 km.

Examining snapshots of the 3D volume at different times can provide valuable insights into the evolution and shape of plasma parameters under the influence of a constant current density driver. Figures 7 and 8 display the total plasma density at 03:00 and 07:00 min, respectively. Each figure is divided into four panels: panel (a) presents a longitudinal cut at the center longitude of the flow channel, panel (b) provides a latitudinal cut along the magnetic field line, and panels (c) and (d) offer altitude cuts at 120 and 240 km, respectively. These figures illustrate how the plasma density on the north side is enhanced by the precipitation on the upward part of the current density, and how the depletion at the center of the channel is concentrated between 100 and 150 km. The channel's behavior on the longitudinal coordinate is somewhat uniform, but with a taller plasma depletion on the eastern side. The plasma depletion spans the entire longitudinal length at 120 km, with the depletion somewhat choked at the eastern edge. At 240 km, the plasma depletion is yet to be significant. Supporting Information S1, including movies showing all plasma parameters (Movies S1–S17), is available for further examination.

In comparison, Figures 8a and 8b demonstrate how the F-region has begun to deplete, a phenomenon that is expected and also corroborated by DMSP measurements (Nishimura, Donovan, et al., 2020). The extent of the depletion volume is now much larger compared to Figure 7, and the eastern side once again exhibits its plasma depletion tapering to lower altitudes. Figure 8c further reveals that the eastern side of the plasma depletion is narrower than at other longitudes. This can be explained by the fact that in our 3D simulation, new plasma is being fed into the channel from the east at a constant rate. This is a critical physical behavior that is missing from 2D simulations. From Movie S1 and the previous snapshots, it is more appropriate to say that the growth is damped rather than choked after the fact. Figure 8d shows how the plasma depletion at 240 km is of an order of magnitude, becoming wider as we move from the eastern edge toward the west.

Indeed, by examining the channel velocity, we can appreciate the "traveling" of its maximum value. Figures 9 and 10 display the east-west channel velocity at 03:00 and 07:00 min, respectively, with the panels representing the same locations as in Figure 7. By comparing the results on panel (b) in both Figures 9 and 10, it becomes clear that the maximum velocity starts on the eastern side and ends on the western side. This is an expected result since the eastern side of the grid has had more time for the plasma to recombine, thus having lower densities than the

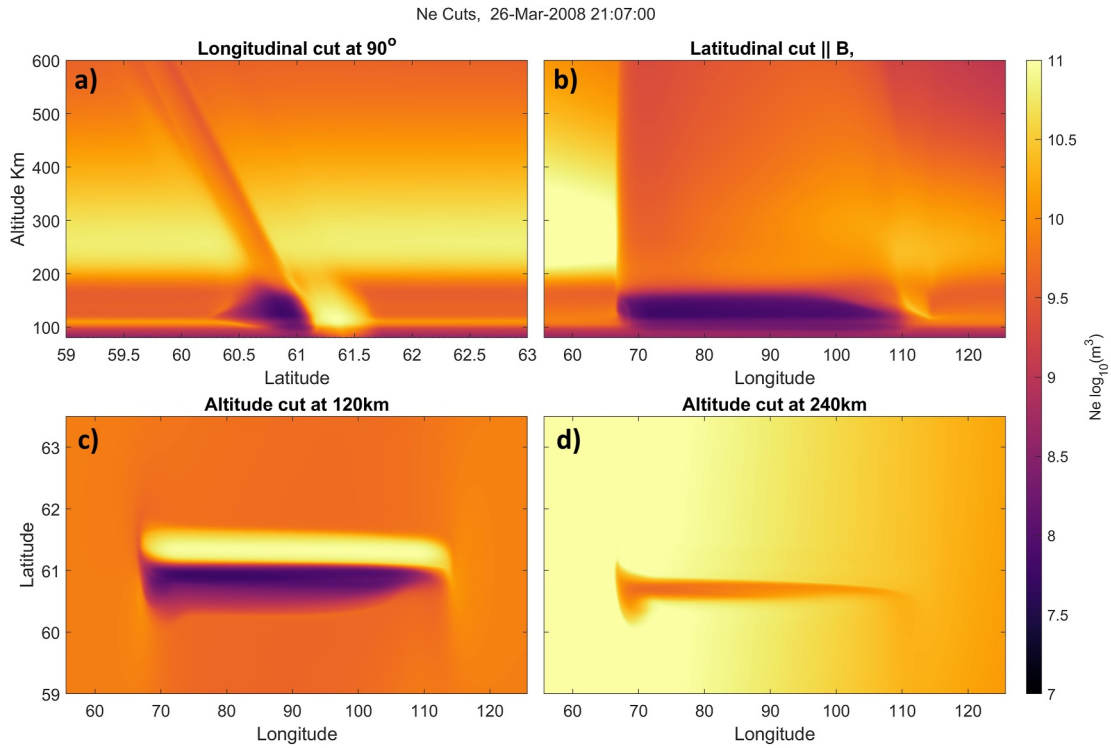

Figure 8. Plasma density at 07:00. All locations in latitude, longitude and altitude are the same as the ones shown on Figure 7.

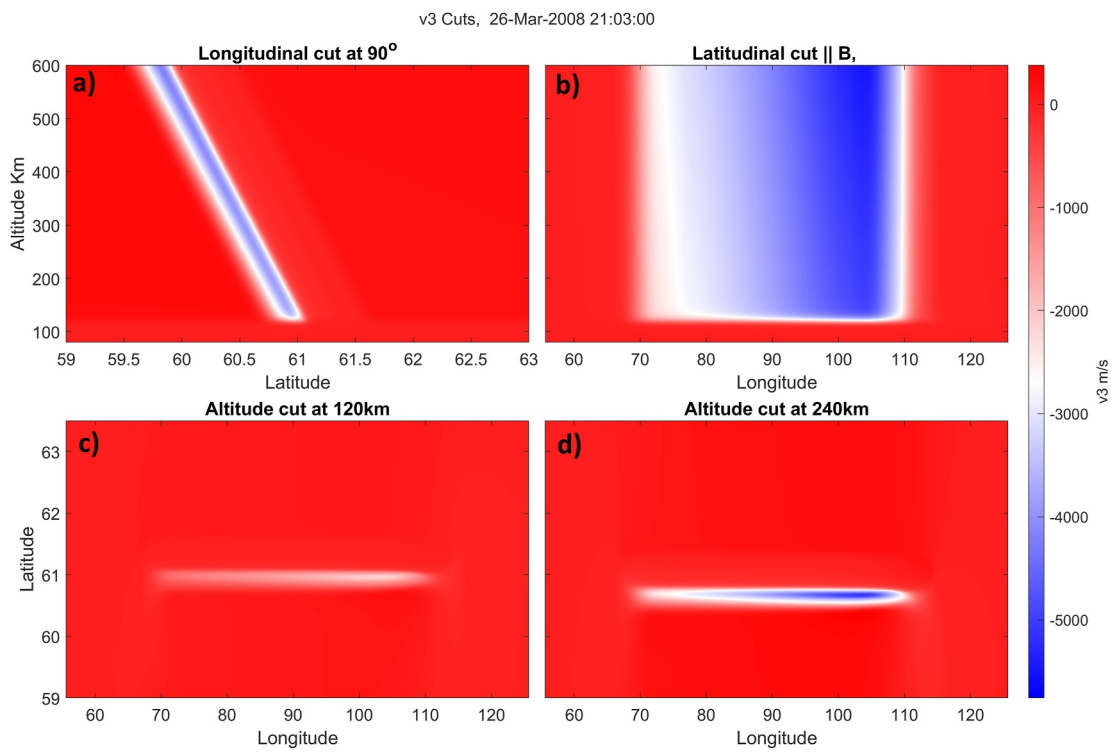

Figure 9. Channel east-west velocity at 03:00. All locations in latitude, longitude and altitude are the same as the ones shown on Figure 7.

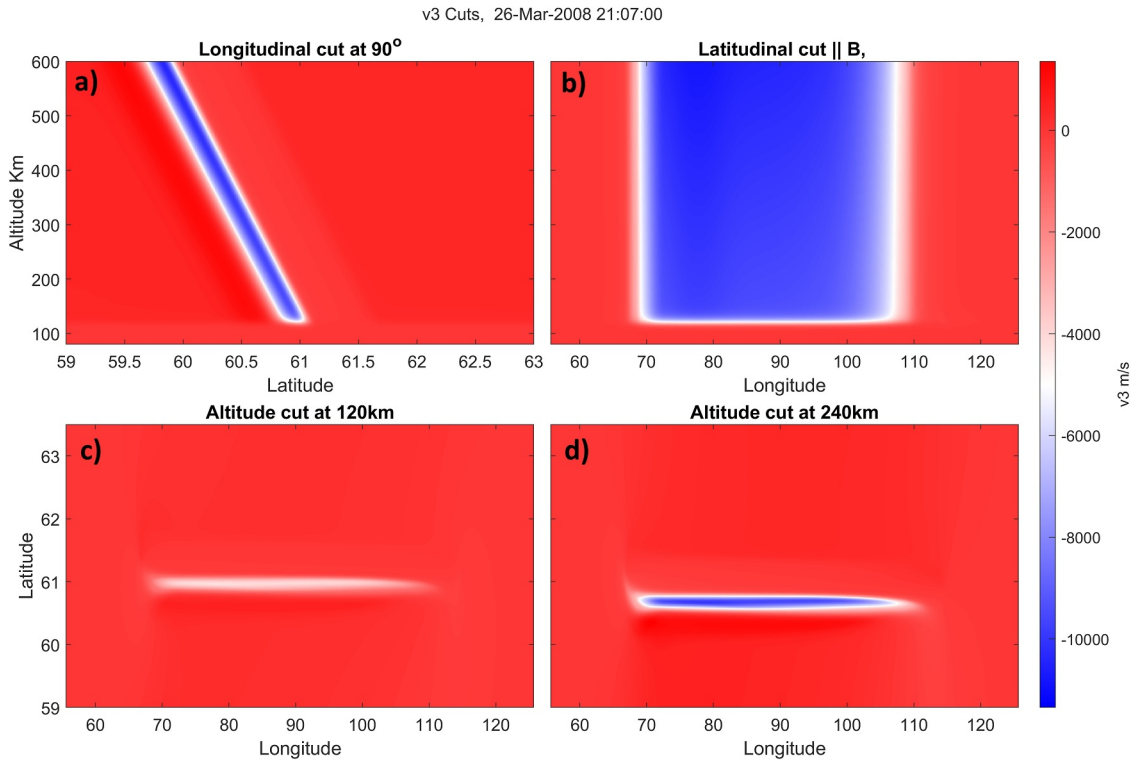

Figure 10. Channel east-west velocity at 07:00. All locations in latitude, longitude and altitude are the same as the ones shown on Figure 7.

western side and reaching a larger plasma depletion first. Later on, the western side catches up, and the velocity maximum shifts to the western side. The width of the channel is approximately 0.5° in latitude, though its size is not perfectly uniform in longitude. This channel width agrees with the measurements presented by Nishimura, Donovan, et al. (2020).

Finally, we should pay attention to the extreme electron temperatures that the simulation predicts between 100 and 150 km. Figure 11 shows the electron temperature at 07:00 min in the same panel configuration as previous figures. This enhanced electron temperature happens in the same area where the plasma is extremely depleted, making the definition of temperature itself somewhat complicated. As previously stated, above 7,000 K the electron-neutral collisions grow unbound a linearly with temperature, and the positive feedback that exist on the frictional heating term makes the electron temperature grow unbound as well.

This also has an effect on the current density at lower altitudes. As shown in Figure 2, current density is flowing at 100 km altitude, and this current is caused by the interplay between the enhancement in temperature causing larger collision frequencies, large enough that the collision frequency matches, and even surpasses, the electron cyclotron frequency, thus making the electrons collide in a small band. Figure 12 shows how the electron temperature and the closure current density change in time and longitude at 110 and 100 km respectively. Lines are also included to show the different thresholds defined previously. The increase in electron temperature on Figure 12(top) does follow the same behavior of starting in the east, with its maximum value traveling toward the west as time moves on. It also closely follows how the channel velocity behaves as seen on Figure 5(top), and therefore it is following the electric field caused by the driving current density. This confirms the fact that our uncapped collision frequencies are indeed the culprit for the enhanced electron temperature. Figure 12(bottom) shows how the closure current density at 100 km has almost the same behavior as the channel acceleration, with it growing and decaying in a peak-valley-peak configuration also seen in Figure 5(bottom).

3.2. Comparison to 2D Simulation

As previously mentioned, there have been attempts to simulate an extreme SAID channel in 2D. Specifically, Liang et al. (2021) simulated an extreme SAID in 2D with a focus on potential generation, while in a subsequent

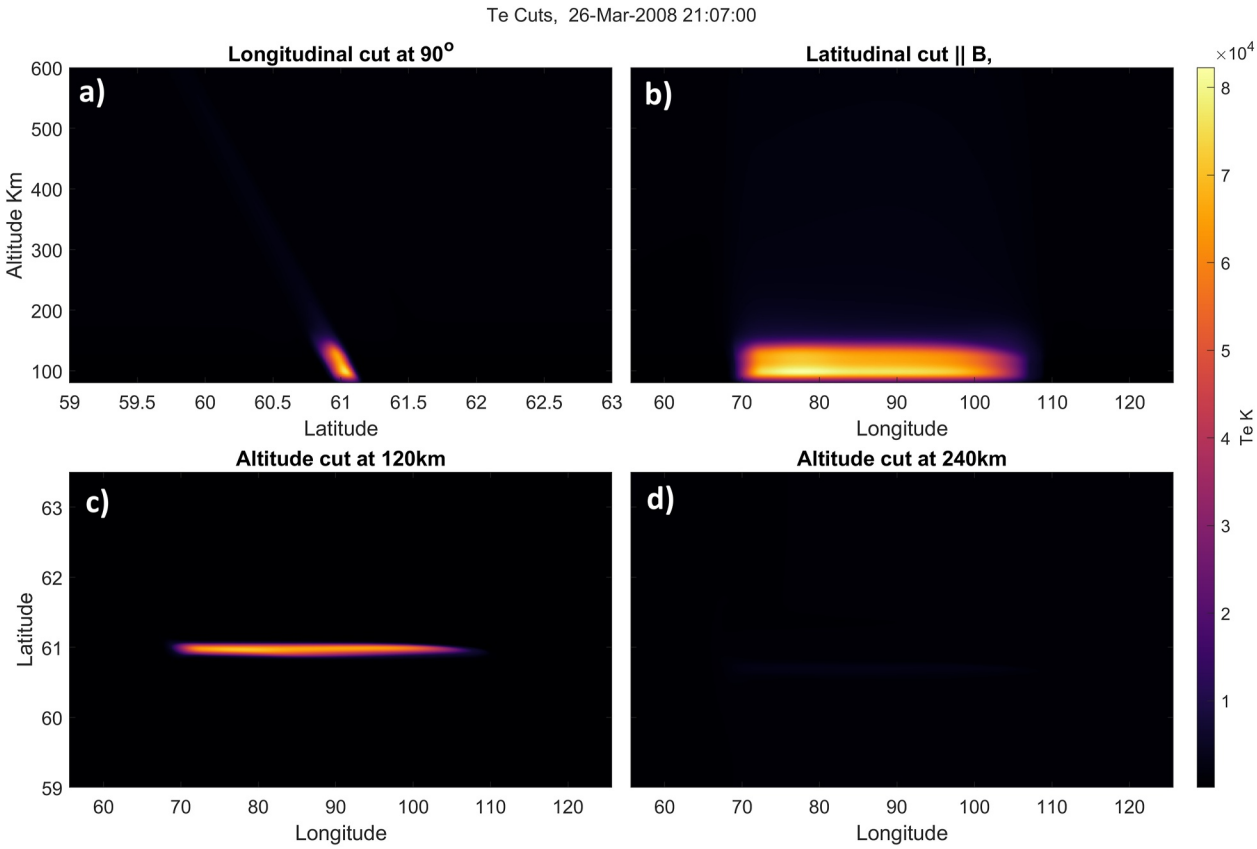

Figure 11. Electron temperature at 07:00. All locations in latitude, longitude and altitude are the same as the ones shown on Figure 7.

paper, Liang et al. (2022) employed a current generation method. To directly compare 2D and 3D simulations, we established a GEMINI framework in 2D. The longitudinal coordinate was reduced to a single cell, and the driving current was adapted to match the pattern shown in panel (a) of Figure 2 and Equation 1, while maintaining the same grid size and other input parameters. Supporting Information S1 for the 2D simulations can be seen on Figures S20–S25 in Supporting Information S1 and Movies S18–S20.

Figure 13 presents 2D simulation results, focusing on field-aligned profiles at the flow channel center, at the same location as Figure 2. Lines are also included to show the different thresholds defined previously. Similar to the 3D simulation, the companion Figure 14 specifically focuses on channel velocity, temperatures, specific ion densities, growth rates in velocity and temperature, as well as height-integrated conductivity. As before, the initial 5 s of the simulation do not have any current driver applied, with J_1 growing linearly during the subsequent 5 s to a value of approximately 0.6 μA/m^2, remaining constant for the rest of the simulation, as shown in panel (a) of Figure 13. The east/west velocity of the channel displayed in Figure 13 demonstrates that the channel velocity reaches 1 km/s at 00:10, just like the 3D case. Figures 14a and 14b illustrate that there are some phases that can be divided into the peak-valley-peak configuration that the 3D simulations showed, though they are much more subdued and are only visible in the acceleration panel. The velocity appears to grow constantly, reaching an extreme value of 21.6 km/s by the end of the simulation. After 8 min, aligning itself with the end of the 3D simulation, the 2D velocity of the channel is 15 km/s, 50% larger than its 3D counterpart at a maximum of 10 km/s. The section will therefore focus on the differences between the two simulations.

The first discernible phase begins at 00:10 min and ends approximately at 02:10 min, as depicted in Figures 3a and 3b, which aligns remarkably with the time frames of the 3D simulation. The velocity and acceleration of the channel follows the same behavior as the 3D case, with less than 100 m/s difference. Once again, the end of the phase closely aligns with the point where $[NO^+]$ and $[O^+]$ are within an order of magnitude of each other at 240 km. During this first phase, analogous to the 3D case, we have that $\left[O_2^+\right]$ reaches the threshold energy needed

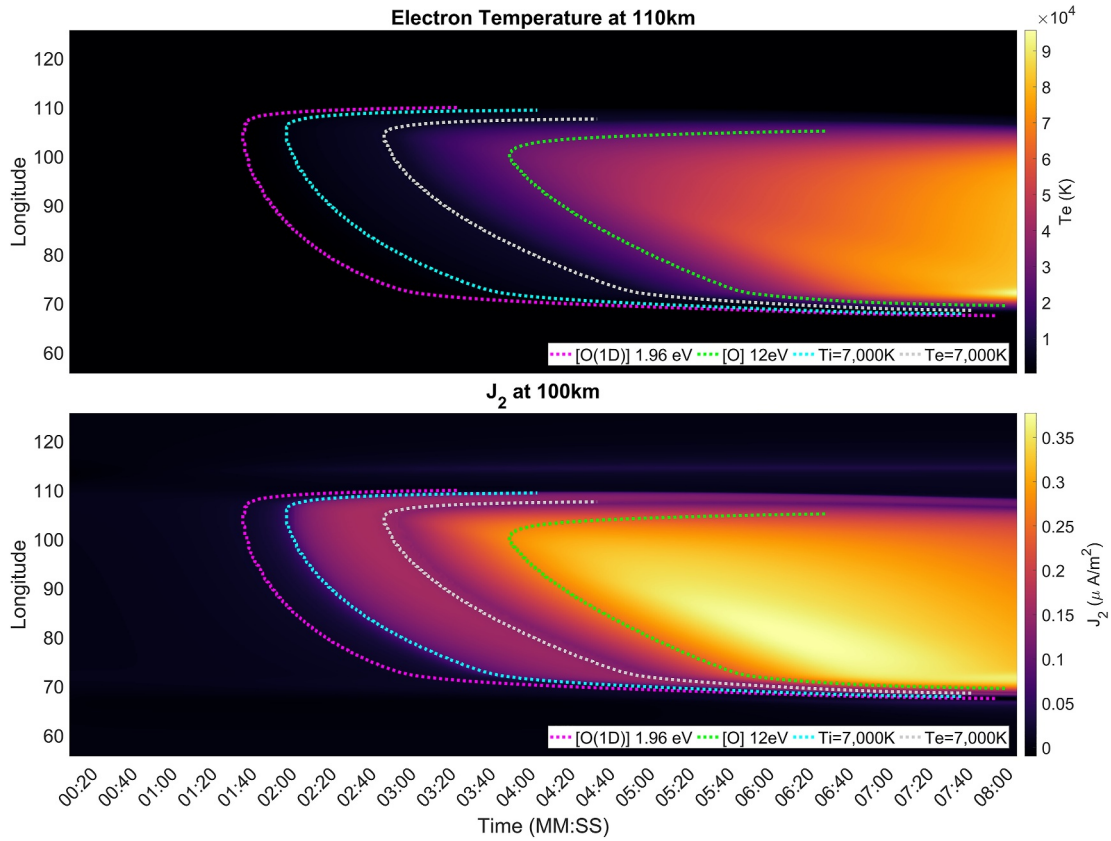

Figure 12. Electron temperature (top panel) and closure current at 100 km (bottom panel). *Y* axis represents longitude at the center of the channel. Simulation starts when the 90° longitude point reaches 21 MLT.

for the O(^{1}D) excitation state to happen at about 01:55. Which means that from that point on, energy will be lost to inelastic collisions, decreasing the channel velocity without affecting the electric field. The lower F-region also reaches ion temperatures above 7,000 K at approximately 02:00, with the average ion temperature between 150 and 400 km reaching the same value later a 02:25, affecting the losses due to rotational and vibrations modes of $[N_2]$ and $[O_2]$.

The second phase spans from 02:10 min to 03:50, which is considerably longer than the 3D case. From Figure 13a, it is evident that the channel velocity and acceleration are no longer similar to those in the 3D case. The channel velocity steadily increases, reaching 4.8 km/s by the 03:50 min mark, which is significantly smaller than the 5.8 km/s shown by the 3D simulations at the same time. From Figure 14a, we observe that the electron temperature behaves in the same way as in the 3D case. From Figure 14b, it is apparent that even though the shape of the peak-valley-peak is somewhat preserved, the large differences in the maximum values and time frames result in a channel that is very different in terms of velocity.

Finally, our last phase, which commences at 03:50 min and continues until the end of the simulation, illustrates how the differences from the 3D version become much more pronounced and extreme. As depicted in Figure 13a, the channel velocity consistently increases, reaching 21.6 km/s by the end of the simulation. From Figures 13b and 13c, the electron temperatures reaches an extreme value of 167,000 K. The closure current primarily flows at 180 and 100 km from 03:50 onwards, as seen in Figure 13d. Figures 14a and 14b convey the same narrative, with a constant increase in channel velocity, temperatures, acceleration, and temperature growth. Unlike the 3D simulation, there is no decrease in acceleration. Figure 14c reveals some of the reasons for such a stark difference: the plasma densities of $[NO^+]$ and $\left[O_2^+\right]$ in the E and F-region never reach a steady state and constantly decrease over time, attaining lower values than in the 3D simulation.

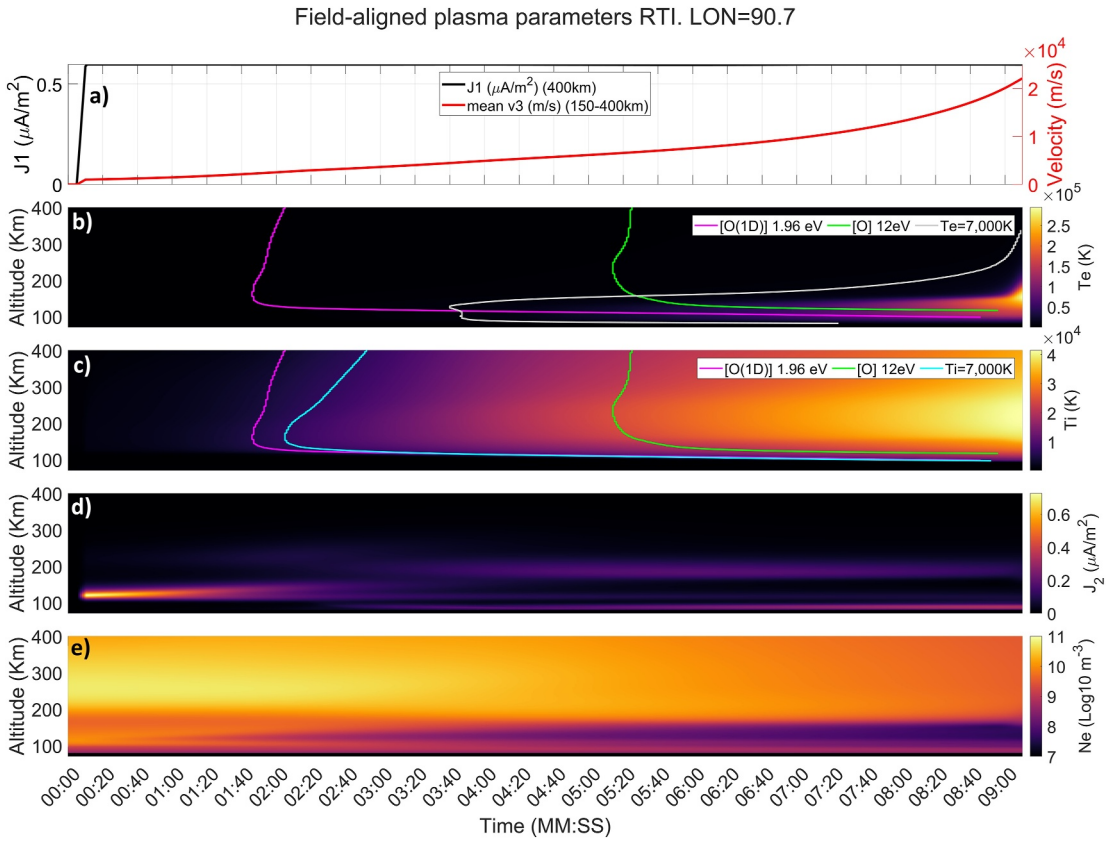

Figure 13. Field-aligned profiles are taken at the center of the flow channel for a 2D simulation. Panel (a) displays values for parallel-to-B current density (J_1) and east/west velocity (v_3) at averaged from 150 to 400 km. Panels (b) and (c) showcase electron (T_e) and ion (T_i) temperatures, respectively. Panel (d) depicts the north/south current (J_2), while panel (e) provides insights into the total electron density (N_e).

The plasma density of $[O^+]$ exhibits the same trend, with a constant decrease in density which does reach a certain constant value, whereas the 3D version experienced an increase in it. These differences in plasma densities and temperatures significantly impact the height-integrated conductance, as it falls below the 3D case by the end of the simulation, as seen in panel d), with a final value of 0.018 S compared to 0.026 S for the 3D case.

At the 05:20 min mark the threshold for $\left[O_2^+\right]$ becoming 12 eV is reached. It is expected then that plasma will start to be generated in E-region above 115 km, affecting the conductance and thus limiting the maximum value of the channel velocity. In comparison to the 3D case, which had ionization from 120 km upwards, the E-region will have more density generated, therefore a larger conductance and finally a larger decrease in the channel velocity.

4. Discussion

This study presents a time-dependent 3D simulation of an extreme SAID channel, aiming to elucidate the emergence of the STEVE phenomena. Our focus lies in the lower F-region and the E-region, where direct experimental measurements are currently absent. Due to STEVE's wandering behavior, there exist few, if any, rocket or radar measurements, necessitating reliance on sparse satellite measurements between 400 km (SWARM) and 850 km (DMSP). From these measurements, we developed a 3D simulation driven solely by the current density on the grid's upper boundary. We made necessary modifications for the simulation to operate under the extreme conditions where the STEVE phenomena are presumed to exist and simulated the ionospheric changes due to such current density. We demonstrated the validity of the current generation method to create an SAID, as explained by Anderson et al. (1993) and their subsequent work. We established a direct relationship between the current density value and shape driving the system and the velocity of the generated SAID channel. Using the results of Nishimura, Donovan, et al. (2020) as an initial reference, we drove the system with current densities approaching over 0.6 μA/m^2. Our current driver mechanism, shape in space as well as the values for

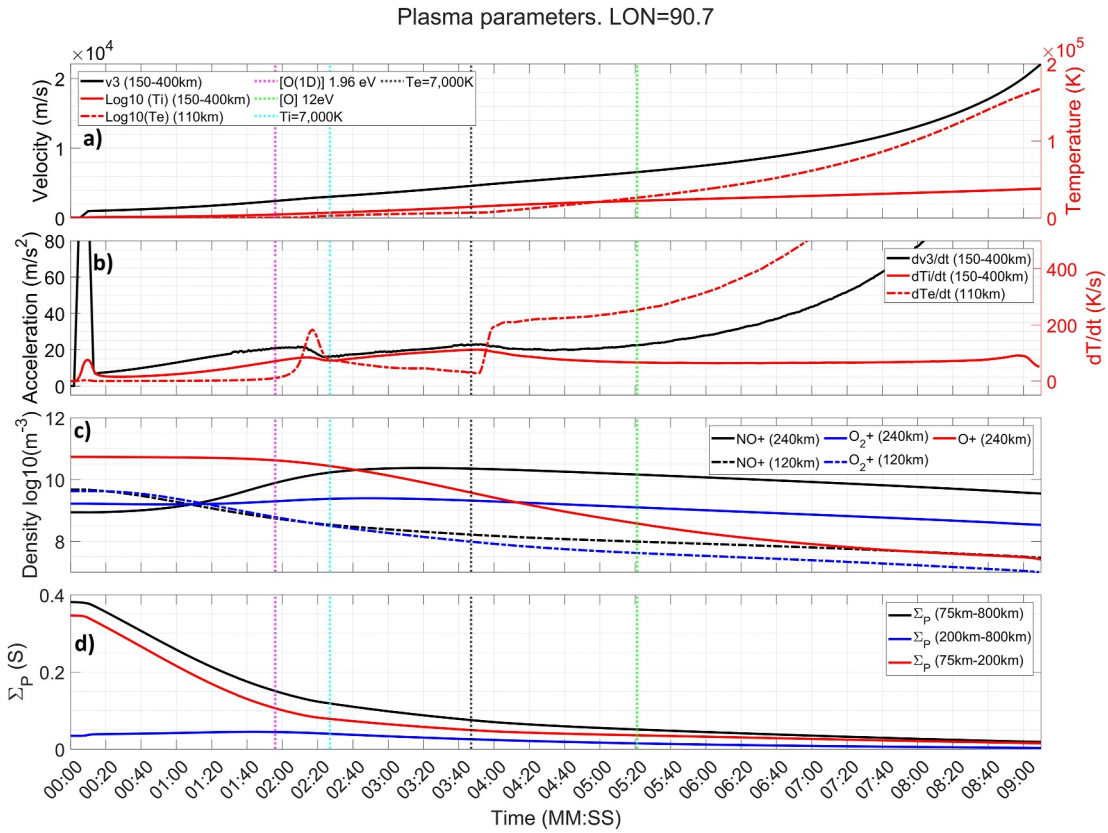

Figure 14. Miscellaneous output parameters of a 2D simulation. Panel (a) shows the average channel velocity (v_3, solid black line) and ion temperature (T_i, solid red line) between 150 and 400 km, as well as the electron temperature (T_e, dashed red line) at 120 km. Panel (b) shows the time derivative of all variables shown on panel (a). Panel (c) shows the density of the main ions, $[NO^+]$ and $\left[O_2^+\right]$ at 120 km (black and blue solid lines) and 240 km (black and blue dashed lines) as well as $[O^+]$ at 240 km (solid red line). Panel (d) shows the total height integrated Pedersen conductance (Σ_p, solid black line), as well as the F-region (200–800 km, solid blue line) and E-region (95–200 km, solid red line) contribution.

precipitation in the upward section of the FAC were all taken from the work done by Liang et al. (2022), which served as the main inspiration for this work.

We managed to produce flow velocities up to 10 km/s, exceeding the 4.5 km/s measured by DMSP, and observed larger ion and electron temperatures than those measured. The increase in the channel velocity during its initial existence is primarily due to the decrease in conductance caused by the current density closing through the E-region, although this decrease is not unbounded. We showed that the entire F-region is not fully depleted as the simulation progresses. The densities of the main ions reach a steady state after a few minutes, maintaining the closure current at a higher altitude and entirely avoiding the E-region. Consequently, there is not a linear increase in velocity throughout the entire simulation, only while the E-region is being strongly depleted. The primary reason for this behavior is the suppressed growth in $E \times B$ drift on the eastern side, here new plasma is introduced into the channel. On the eastern side, plasma sources and a clockwise velocity vortex pinch the channel, reducing its longitudinal length and preventing the plasma density from depleting. Our 3D SAID channel was a longitudinal width of approximately 40° (2,200 km at the selected latitude), which means it spans almost three different hours in MLT. This results in the western edge of the simulation being at 7:20 MLT at the start of the simulation, with the eastern edge at 10:40 MLT. The faster velocity and higher temperatures in the dusk side coincide with the existence of STEVE being more prevalent toward the dusk side, with the midnight sector being less extreme (Nishimura, Yang, et al., 2020).

Our simulations provide insight into how the driving factors affect an extreme SAID flow channel. Starting with the current density, a larger value leads to a larger steady-state channel velocity. A larger current density implies a larger electric field for a constant conductivity. However, this is not the only factor that influences the behavior of the channel velocity. The longitudinal length also has a direct relationship with it, with a longer channel in

longitude producing larger velocities. Our raised cosine shape for the longitudinal characteristics of the current density enabled us to alter the length in longitude at which the driving current is at its maximum value. Consequently, the longer the current is at its maximum, the greater the channel velocity. We conducted some simulations with the inclusion of a blanket background precipitation. This did not eliminate the channel but rather extended the time frames at which events occur and marginally limited the flow channel velocity. The final modification to the driving factors was the width of the channel in latitude, with a wider channel exhibiting larger velocities for the same current density. However, this is not entirely realistic, as we expect that in a wider channel, the current density will be much smaller and fall into the SAPS category.

We also showed in detail how are simulations are lacking inelastic collisions and impact ionization, and how the threshold for these two events (1.96 eV for $O(^1D)$ excitation state and 12 eV for $[O]$ ionization) happens in time and space. Both this threshold will provide means for slowing the channels velocity growth, thus the 10 km/s final velocity must be considered more of a reference than a real channel velocity. Threshold for temperatures going above what the current equations boundaries are where also included, and allowed us to see why the phases happen they way they do.

The decision not to cap the electron temperature when calculating collision frequencies between electrons and neutrals that positively depend on the electron temperature is nuanced. Both approaches exist outside of any measured or theorized physics, rendering them both flawed. We chose to leave these temperatures uncapped since our results would exist outside the current understanding of the collision processes occurring in the E-region, regardless of the approach. The only temperatures capped were those that negatively depend on the electron temperature, as these would generate negative collision frequencies and cause the model to error out upon reaching such temperatures. As a direct consequence of this decision, we have current flowing at 100 km, where the collision frequency between electrons and neutrals (particularly molecular oxygen) becomes higher than the local electron cyclotron frequency. This implies that the electric field necessary to drive the closure current density to flow northward is smaller than if we had decided to cap the temperatures. If the enhancement of Pedersen conductivity at 100 km does not exist, the current density still needs to close through the sparse E-region plasma available and the lower F-region plasma. This, in turn, means that the electric field would need to be even larger to allow for more current to flow under such a change in Pedersen conductivity, resulting in a faster channel velocity, larger energies for $[NO^+]$ and $\left[O_2^+\right]$, and pushing the simulation even further from our known physics formulas of temperature, collision frequencies, and transport.

Lynch et al. (2022) and Liang et al. (2021) both utilized an electric field driver, which allowed the current density to adjust itself to whatever is needed for such driving potential. We argue that the current-driver is a better representation of M-I coupling, allowing the electric field to adjust itself to a value that allows such a current density to exist. Even this assumptions has it drawbacks, as the conditions and details of where current is closing under these extreme conditions is not well known. At the same time, a constant current density at the top of the grid might not be the best approximation, as current variations are known to exist and are related to the ring current itself. As such our model predictions will require validation from further measurements of campaigns. As mentioned before, what is needed is an Alfvenic boundary condition inside GEMINI Wright and Russell (2014).

4.1. Role of 3D Over 2D Simulations

We have also conducted 2D simulations using the same driving factors as their 3D counterparts in order to directly compare our results to the ones obtained by Liang et al. (2021, 2022). From these, we learned that during the initial time frames, the channels behave similarly between 2D and 3D, with the main phases of the channel existing present. However, the differences become stark thereafter. In the absence of the longitudinal coordinate, the channel grows without bounds, with the plasma density being depleted at all altitudes. Thus, the conductance reaches incredibly low values and is constantly decreasing, unlike in the 3D simulation. Liang et al. (2022) shows this extreme depletion of density being almost half an order of magnitude larger than our 3D simulations. The 3D simulation of the extreme SAID flow channel has provided numerous insights into the complex dynamics of this phenomenon. The results have revealed intricate structures and behaviors that are inherently three-dimensional, underscoring the importance of using 3D simulations for such studies. This added complexity can yield more accurate and realistic results. However, it also introduces more complexity into the simulation and the subsequent analysis of the results. Both our 2D and 3D simulations did not include the electron heat flow that is expected from the magnetosphere, which was an inclusion in the work of Liang et al. (2021, 2022). Our reason for leaving the

input aside was to encapsulate the effects of the extreme SAID by itself, with the heat flow being an input that will be added later on. This is the reason for the differences in our electron temperature versus the ones published by Liang et al. (2021, 2022), at least in the F-region. In the E-region, our temperatures are larger than the ones obtained by Liang et al. (2021, 2022) due to our unbound collision frequencies as explained in Section 4. Ion temperatures on the other hand, which are tied directly to the channel flow, share large similarities between them, which is expected since the differences in velocities reaches at best 100%.

Choosing between 2D and 3D simulations involves trade-offs. One of the main considerations is that 3D simulations require significantly more computational resources than 2D simulations. They involve more data points, leading to increased memory requirements, and more computations per time step, which escalates the processing power and time needed. This can be a limiting factor, particularly for complex systems or simulations that span long periods. While 2D simulations can offer valuable insights and are often employed for initial explorations, they may not fully encapsulate the behavior of systems that are inherently 3D, leading to a loss of information due to the collapse of one dimension. In such instances, 3D simulations can provide a more accurate representation. However, visualizing and interpreting the results of 3D simulations can be more challenging than for 2D simulations due to the additional dimension and the constraints of 2D plots. On the other hand, this simplification can distort the representation of the system, especially when the collapsed dimension contains critical information. 3D simulations retain all spatial information, offering a more comprehensive and accurate depiction of the system.

One of the most striking findings from the 3D simulation is the presence of significant structure in the longitudinal coordinate which is not present on the 2D simulations made by Liang et al. (2021, 2022). This structure has a profound impact on the behavior of the SAID channel, specifically the plasma sources and flows that seem to constrain the channel growth in the east. These structures play a pivotal role in shaping the dynamics of the SAID channel, influencing its velocity and temperature. Since 2D lacks the new plasma coming into the channel from the longitudinal direction, the plasma depletion is unbounded and reaches values much lower than its 3D counterpart. This is especially important in the F-region, where most of the current flows after the E-region is completely depleted. This in part allows the conductance to decrease to very small values which, in turn, increases the electric field in order to maintain a constant current through the system.

4.2. On the Need for Future Improvements to Modeling

While this study has addressed 3D structure of flow channels, the simulations presented herein should be interpreted as approximate in only a very rough sense for a number of reasons. Foremost there are relatively few observations that allow us to constrain the model inputs so it is not clear whether we are simulating a somewhat typical STEVE event or one of the most extreme events ever observed. It should also be noted that a number of assumptions needed to be made in order to even achieve sensible results in our model—some of which could impact the ionospheric behavior substantially. These largely concern parameterizations of collisional processes (cf. Section 2.2) which apparently become invalid at the energies required for our analysis. We have chosen to calculate these collisional processes using a temperature with a set ceiling; however, a more physically motivated extrapolation would be preferable for future studies in such extreme conditions. Finally, ion energies that result from our modeling are well above the limits that would trigger inelastic ion-neutral and ion-ion collisions—these are not included presently (it is not clear whether the requisite cross-section data are even available) but likely represent an important energy sink that will limit temperatures.

5. Summary and Future Work

The presented study demonstrates our ability to simulate an extreme SAID channel, with results surpassing the current measurements of STEVE. The simulations unveiled intricate structures and behaviors, underscoring the significance of 3D simulations in capturing these phenomena. The correlation between plasma depletion, conductance increase, and channel velocity increase is validated, even at the extreme velocities of 10 km/s. The research also highlights the influence of various factors, such as current density and longitudinal length, on the behavior of the channel velocity. However, these simulations should be considered as approximations due to the scarcity of observations available to constrain the model inputs and the assumptions made to obtain plausible results. Simulation results produce features that are qualitative consistent with optical and space-based observations, while exposing the physical limitations of current models used in SAID-STEVE studies. We show that a plausible ionosphere created by driving it with measured STEVE drivers rapidly reaches parameter values that are

beyond the limits of applicability of the governing equations, and beyond known physical limits of the key collisional models used. In particular, effects of inelastic collisions and impact ionization will likely become an important consideration in STEVE.

We pushed GEMINI to the boundaries of what is stable, as well as made assumptions about collisional terms that might affect the final results. The way the simulation was set up leaves us with many important points that must be remembered:

- A 3D grid was utilized that followed a tilted dipole coordinate system. This grid spans from 0 to 100 km in altitude, 58° to 64° in latitude, and 55° to 125° in longitude. The grid size was set at 512 × 512 × 512.
- The simulation was driven by a field-aligned current density shape as seen on Figure 2. The shape in latitude was chosen as two opposite sign Gaussian's, which allowed us to have and up and down current density with smooth edges, something essential for modeling. Precipitating electrons where added on the upward portion of the current, to simulate a current carried by precipitating electrons. In longitude, a raised-cosine shape was used so that we could have a long and constant longitudinal shape, yet a smooth transition to zero at the edges.
- A maximum value of 0.6 $\mu A/m^2$ for the driving current density was chosen. This agrees with previous measurements, though smaller than what Nishimura, Donovan, et al. (2020) measures.
- GEMINI underwent changes to some of its internal code in order to accommodate the extreme velocities and temperatures. Particularly some electron-neutral collision frequencies had to be capped since at higher temperatures they would become negative.
- GEMINI numerical solver was also adapted to solve its thermal conductivity and source-loss terms simultaneously to avoid oscillations due to the high temperatures.
- Since there are no inelastic collisions nor impact ionization terms in GEMINI, one must consider our results as a reference, in reality these and other kinetic processes are expected to be triggered at these extremes situations.

Our results show how there are distinct phases in time during the creation and existence of an extreme SAID channel, as well as how the phases might be related to the different plasma densities and transport inside the extreme SAID channel. The longitudinal aspect is critical, since the more eastward we are the channel grows faster, while the westward section grows slower but reaches much larger values of velocity and temperature. From our simulations, we can create a list of important results that need to be highlighted:

- The channel velocity grows exponentially, finishing with a linear growth, to values of 10 km/s on the western edge. This values are larger than the ones previously presented by Nishimura, Donovan, et al. (2020), and show how under a current smaller than measured it is possible to obtain extremely large flows. The real value will be smaller than this though, due to the omission of inelastic collisions nor impact ionization terms that will work against channel velocity growth.
- Approximately four phases exist during the 8 min simulation time, not considering the initial 10 s where the driving current density grows fast to its maximum value.
- The first phase can be described as an exponential growth in velocity up to 1 km/s, most of the closure current flows through the 110–130 km region and the E-region is rapidly being depleted. From a few second in, there is enough ion temperature to trigger the most important reaction: $[O^+] + [N_2] \rightarrow [NO^+] + [N]$ which depletes the $[O^+]$ in the lower F region. During this phase inelastic collisions will start to happen, thus decreasing the velocity due to energy being soaked up.
- A second phase happens between two local maxima of the acceleration of the channel, roughly existing between the points where the ion and electron temperature reach 7,000 K. During this time $[O^+]$ is being rapidly depleted in the F region, while the E-region densities continue their exponential decrease. This section is characterized by a large growth in the acceleration, as well as electron temperature. During this phase we still have valid electron-neutral collision frequencies. The second phase is also characterized by the closure current flowing through other altitudes rather than the 110–130 km region.
- Our third phase only exist on the westward portion of the channel, with its end coinciding with the point where the density of $[O^+]$ in the F-region reaches the values of the density of plasma in the E-region. It has the largest acceleration compared to other phases. At this point, we have a total 400 mV/m^2 electric field. The electron temperature is now larger than 7,000 K, thus the collision frequencies grow unbound, affecting the frictional heating. During this phase $\left[O_2^+\right]$ reaches 12 eV, enough energy to ionize the ambient $[O]$, creating plasma from 120 km upward and thus increasing the conductance, reducing the channel velocity in turn.

- The final phase exist on all locations in terms of longitude, and it is characterized by a constant and linear growth of the channel velocity, with a smaller slope than any other previous phase, confirmed by the much lower and constant acceleration. Densities of $[NO^+]$ and $\left[O_2^+\right]$ in the F-region reach a steady state where they remain mostly constant. There is a slow increase of $[O^+]$ in the F-region. We are outside the boundaries of most validity for most equations at this point.

From these phases and the behavior of the channel in both latitude and longitude, several important points can be made about how our simulation attempts to model the behavior of STEVE through an extreme SAID flow channel. From this, we can create a list of key takeaways from the simulations:

- This study has utilized 3D simulations to explore the dynamics of extreme SAID flow channels, with a focus on the STEVE phenomena.
- The simulations have revealed complex structures and behaviors, emphasizing the importance of 3D over 2D simulations in capturing these phenomena.
- Under a constant current density driver, the channel growth in velocity is not uniform. Fast velocities are reaches in the eastern side first since it has less plasma to deplete due to plasma recombination. Western side grows slower due to the larger plasma in that region, but reaches velocities up to 10% higher than its opposite side.
- We predict testable changes in the ionosphere-thermosphere-magnetosphere system response when the temperature exceeds the turn-on threshold for the $[O^+] + [N_2]$ reaction.
- Chemistry in the E-region and lower F-region controls the channel velocity behavior. Once the E-region becomes almost completely depleted, current flows through the lower F-region.
- The omission of inelastic terms helps the channel to grow even more than what it would in real life. Same can be said about the impact ionization effect on the conductance.
- Temperature threshold are very important. In our case, since we left the collision frequencies between electrons and some neutrals uncapped if they would not reach negative values, we have an abnormal electron temperature increase in the E-region. It does not expand to higher altitudes since it depends mostly on the density of $[O_2]$. This causes the electron-neutral collision frequency to rise above the electron cyclotron frequency in a small band at 100 km, allowing current to flow there. If the collision frequencies were capped, we expect the electric field to adjust itself to close the full amount of the current density through the lower F-region, resulting in an even faster flow channel.

5.1. Future Work

We have demonstrated a 3D simulation of an extreme SAID channel in GEMINI, although several constraints were necessary for the model to operate within its limits. It is crucial to revisit the formulas and theories of collision frequencies/collision cross-sections of various ion-neutral and electron-neutral interactions. In this study, only the collision frequencies that would result in a negative number had their temperature capped at a maximum value, while others were left unbounded. The decision to cap or not cap the temperature in all calculations is complex, as both approaches make strong assumptions on what is happening in the ionosphere.

The Geospace Dynamics Constellation (GDC) is a mission concept designed to study the coupling between the magnetosphere and the ionosphere/thermosphere system, which would include plasma drift sensors and more. The results that can be obtained by modeling the ionospheric behavior under an extreme electric field will be useful when searching for signatures of STEVE in GDC data. Conversely, the presence of a sub-auroral phased array incoherent scatter radar, such as AMISR, for example, would provide the necessary data at lower altitudes to further understand the process of STEVE. This study allows us to conduct numerical experiments useful for the design of new instruments and networks. In conclusion, our simulations provide a detailed heterogeneous parameter set for comparison with current and future observations, including:

- ISR (Ne, T_e, T_i, ion composition)
- Imaging spectroscopy (ion abundances, electron energy/temperature)
- LEO satellites (GDC, DMSP, SWARM; temperatures, abundances, flows, precipitation)
- Multi-point observations (GDC constellations, camera networks)

Finally, the current simulations do not account for any effects caused by instabilities in the E and F-region. Due to the large electric field, we anticipate that the Farley-Buneman instability will occur between 100 and 120 km,

leading to an increase in the electron temperature and a change in the conductivities. Liang et al. (2021, 2022) incorporated the effects on the electron temperature in their 2D simulations, utilizing the theory developed by St-Maurice and Goodwin (2021). We plan to include the effects of the Farley-Buneman instability in a simulation of an extreme SAID channel using the results of Dimant and Oppenheim (2011a, 2011b) in the near future.

Data Availability Statement

No experimental data is used in this study. Version v1.6.1–372-g969ab4ef (known as FBI version) of GEMINI3D and PYGEMINI used for the 3D and 2D simulations is preserved at https://doi.org/10.5281/zenodo.10783353, available via Creative Commons Attribution 4.0 International and developed openly at https://github.com/jdiazpena/gemini3d (Zettergren et al., 2024).

Acknowledgments
JMDP was supported by NASA Grant 80NSSC20K1356. MZ was supported by NASA Grant 80NSSC21K1354. The work of YN was supported by NASA Grants 80NSSC21K1321, 80NSSC22K0749, 80NSSC23M0193 and 80NSSC23K0410, NSF Grants AGS-1907698 and AGS-2100975, AFOSR Grants FA9550-23-1-0614 and FA9550-23-1-0634, and ISSI Bern/ISSJ-BJ for the "Multi-Scale Magnetosphere-Ionosphere-Thermosphere Interaction" and "Auroral Research Coordination: Towards Internationalised Citizen Science (ARCTICS)" teams.

References

Anderson, P., Carpenter, D., Tsuruda, K., Mukai, T., & Rich, F. (2001). Multisatellite observations of rapid subauroral ion drifts (SAID). *Journal of Geophysical Research*, *106*(A12), 29585–29599. https://doi.org/10.1029/2001ja000128

Anderson, P., Hanson, W., Heelis, R., Craven, J., Baker, D., & Frank, L. (1993). A proposed production model of rapid subauroral ion drifts and their relationship to substorm evolution. *Journal of Geophysical Research*, *98*(A4), 6069–6078. https://doi.org/10.1029/92ja01975

Anderson, P., Heelis, R., & Hanson, W. (1991). The ionospheric signatures of rapid subauroral ion drifts. *Journal of Geophysical Research*, *96*(A4), 5785–5792.

Archer, W., Gallardo-Lacourt, B., Perry, G. W., St.-Maurice, J.-P., Buchert, S. C., & Donovan, E. (2019). STEVE: The optical signature of intense subauroral ion drifts. *Geophysical Research Letters*, *46*(12), 6279–6286. https://doi.org/10.1029/2019gl082687

Archer, W., & Knudsen, D. J. (2018). Distinguishing subauroral ion drifts from birkeland current boundary flows. *Journal of Geophysical Research: Space Physics*, *123*(1), 819–826. https://doi.org/10.1002/2017ja024577

Archer, W., St.-Maurice, J.-P., Gallardo-Lacourt, B., Perry, G., Cully, C., Donovan, E., et al. (2019). The vertical distribution of the optical emissions of a steve and picket fence event. *Geophysical Research Letters*, *46*(19), 10719–10725. https://doi.org/10.1029/2019gl084473

Banks, P. (1966). *Charged particle temperatures and electron thermal conductivity in the upper atmosphere scientific report no. 276* (Tech. Rep. No. No. NASA-CR-78936). Ionospheric Research Laboratory, The Pennsylvania State University.

Bilitza, D., Pezzopane, M., Truhlik, V., Altadill, D., Reinisch, B. W., & Pignalberi, A. (2022). The international reference ionosphere model: A review and description of an ionospheric benchmark. *Reviews of Geophysics*, *60*(4), e2022RG000792. https://doi.org/10.1029/2022rg000792

Blelly, P., & Schunk, R. (1993). A comparative study of the time-dependent standard 8-, 13- and 16-moment transport formulations of the polar wind. *Annales Geophysicae*, *11*(6), 443–469.

De Keyser, J. (1999). Formation and evolution of subauroral ion drifts in the course of a substorm. *Journal of Geophysical Research*, *104*(A6), 12339–12349. https://doi.org/10.1029/1999ja900109

Dimant, Y., & Oppenheim, M. (2011a). Magnetosphere-ionosphere coupling through E region turbulence: 1. Energy budget. *Journal of Geophysical Research*, *116*(A9). https://doi.org/10.1029/2011ja016648

Dimant, Y., & Oppenheim, M. (2011b). Magnetosphere-ionosphere coupling through E region turbulence: 2. Anomalous conductivities and frictional heating. *Journal of Geophysical Research*, *116*(A9). https://doi.org/10.1029/2011ja016649

Emmert, J. T., Drob, D. P., Picone, J. M., Siskind, D. E., Jones, M., Jr., Mlynczak, M., et al. (2021). Nrlmsis 2.0: A whole-atmosphere empirical model of temperature and neutral species densities. *Earth and Space Science*, *8*(3), e2020EA001321. https://doi.org/10.1029/2020ea001321

Foster, J., Buonsanto, M., Mendillo, M., Nottingham, D., Rich, F., & Denig, W. (1994). Coordinated stable auroral red arc observations: Relationship to plasma convection. *Journal of Geophysical Research*, *99*(A6), 11429–11439. https://doi.org/10.1029/93ja03140

Foster, J., & Burke, W. (2002). Saps: A new categorization for sub-auroral electric fields. *Eos, Transactions American Geophysical Union*, *83*(36), 393–394. https://doi.org/10.1029/2002eo000289

Gallardo-Lacourt, B., Liang, J., Nishimura, Y., & Donovan, E. (2018). On the origin of STEVE: Particle precipitation or ionospheric skyglow? *Geophysical Research Letters*, *45*(16), 7968–7973. https://doi.org/10.1029/2018gl078509

Gallardo-Lacourt, B., Nishimura, Y., Donovan, E., Gillies, D., Perry, G., Archer, W., et al. (2018). A statistical analysis of STEVE. *Journal of Geophysical Research: Space Physics*, *123*(11), 9893–9905. https://doi.org/10.1029/2018ja025368

Galperin, Y. I., & Zosimova, A. G. (1974). Plasma convection in polar ionosphere. *Annales Geophysicae*, *30*(1).

Gillies, D. M., Donovan, E., Hampton, D., Liang, J., Connors, M., Nishimura, Y., et al. (2019). First observations from the TREX spectrograph: The optical spectrum of STEVE and the picket fence phenomena. *Geophysical Research Letters*, *46*(13), 7207–7213. https://doi.org/10.1029/2019gl083272

Gillies, D. M., Liang, J., Gallardo-Lacourt, B., & Donovan, E. (2023). New insight into the transition from a SAR arc to STEVE. *Geophysical Research Letters*, *50*(6), e2022GL101205. https://doi.org/10.1029/2022gl101205

Harding, B. J., Mende, S. B., Triplett, C. C., & Wu, Y.-J. J. (2020). A mechanism for the STEVE continuum emission. *Geophysical Research Letters*, *47*(7), e2020GL087102. https://doi.org/10.1029/2020gl087102

Huba, J., Joyce, G., & Fedder, J. (2000). SAMI2 is another model of the ionosphere (SAMI2): A new low-latitude ionosphere model. *Journal of Geophysical Research*, *105*(A10), 23035–23053. https://doi.org/10.1029/2000ja000035

Huba, J., Joyce, G., & Krall, J. (2008). Three-dimensional equatorial spread F modeling. *Geophysical Research Letters*, *35*(10). https://doi.org/10.1029/2008gl033509

Itikawa, Y. (1974). Momentum-transfer cross sections for electron collisions with atoms and molecules. *Atomic Data and Nuclear Data Tables*, *14*(1), 1–10. https://doi.org/10.1016/s0092-640x(74)80026-4

Itikawa, Y. (2006). Cross sections for electron collisions with nitrogen molecules. *Journal of Physical and Chemical Reference Data*, *35*(1), 31–53. https://doi.org/10.1063/1.1937426

Jones, D. B., Campbell, L., Bottema, M., & Brunger, M. J. (2003). New electron-energy transfer rates for vibrational excitation of O_2. *New Journal of Physics*, *5*(1), 114. https://doi.org/10.1088/1367-2630/5/1/114

LeVeque, R. J. (2007). *Finite difference methods for ordinary and partial differential equations: Steady-state and time-dependent problems*. Society for Industrial and Applied Mathematics.

Liang, J., Donovan, E., Connors, M., Gillies, D., St-Maurice, J., Jackel, B., et al. (2019). Optical spectra and emission altitudes of double-layer STEVE: A case study. *Geophysical Research Letters*, *46*(23), 13630–13639. https://doi.org/10.1029/2019gl085639

Liang, J., St-Maurice, J., & Donovan, E. (2021). A time-dependent two-dimensional model simulation of lower ionospheric variations under intense said. *Journal of Geophysical Research: Space Physics*, *126*(12), e2021JA029756. https://doi.org/10.1029/2021ja029756

Liang, J., St-Maurice, J.-P., & Donovan, E. (2022). Model simulation of said intensification in the ionosphere under a current generator: The role of ion Pedersen transport. *Journal of Geophysical Research: Space Physics*, *127*(11), e2022JA030960. https://doi.org/10.1029/2022ja030960

Lynch, K. A., McManus, E., Gutow, J., Burleigh, M., & Zettergren, M. (2022). An ionospheric conductance gradient driver for subauroral picket fence visible signatures near STEVE events. *Journal of Geophysical Research: Space Physics*, *127*(12), e2022JA030863. https://doi.org/10.1029/2022ja030863

Lyons, L., Nishimura, Y., & Zou, Y. (2016). Unsolved problems: Mesoscale polar cap flow channels' structure, propagation, and effects on space weather disturbances. *Journal of Geophysical Research: Space Physics*, *121*(4), 3347–3352. https://doi.org/10.1002/2016ja022437

MacDonald, E. A., Donovan, E., Nishimura, Y., Case, N. A., Gillies, D. M., Gallardo-Lacourt, B., et al. (2018). New science in plain sight: Citizen scientists lead to the discovery of optical structure in the upper atmosphere. *Science Advances*, *4*(3), eaaq0030. https://doi.org/10.1126/sciadv.aaq0030

Majeed, T., & Strickland, D. J. (1997). New survey of electron impact cross sections for photoelectron and auroral electron energy loss calculations. *Journal of Physical and Chemical Reference Data*, *26*(2), 335–349. https://doi.org/10.1063/1.556008

Martinis, C., Griffin, I., Gallardo-Lacourt, B., Wroten, J., Nishimura, Y., Baumgardner, J., & Knudsen, D. (2022). Rainbow of the night: First direct observation of a SAR arc evolving into STEVE. *Geophysical Research Letters*, *49*(11), e2022GL098511. https://doi.org/10.1029/2022gl098511

Mishin, E. (2013). Interaction of substorm injections with the subauroral geospace: 1. Multispacecraft observations of said. *Journal of Geophysical Research: Space Physics*, *118*(9), 5782–5796. https://doi.org/10.1002/jgra.50548

Mishin, E., Nishimura, Y., & Foster, J. (2017). SAPS/SAID revisited: A causal relation to the substorm current wedge. *Journal of Geophysical Research: Space Physics*, *122*(8), 8516–8535. https://doi.org/10.1002/2017ja024263

Mishin, E., & Streltsov, A. (2019). STEVE and the picket fence: Evidence of feedback-unstable magnetosphere-ionosphere interaction. *Geophysical Research Letters*, *46*(24), 14247–14255. https://doi.org/10.1029/2019gl085446

Mishin, E., & Streltsov, A. (2022). On the kinetic theory of subauroral arcs. *Journal of Geophysical Research: Space Physics*, *127*(8), e2022JA030667. https://doi.org/10.1029/2022ja030667

Mishin, E., & Streltsov, A. (2023). The inner structure of STEVE-linked SAID. *Geophysical Research Letters*, *50*(8), e2023GL102956. https://doi.org/10.1029/2023gl102956

Mishin, E., & Streltsov, A. (2024). Toward the unified theory of said-linked subauroral arcs. *Journal of Geophysical Research: Space Physics*, *129*(1), e2023JA032196. https://doi.org/10.1029/2023ja032196

Nishimura, Y., Deng, Y., Lyons, L. R., McGranaghan, R. M., & Zettergren, M. D. (2021). Multiscale dynamics in the high-latitude ionosphere. *Ionosphere dynamics and applications*, 49–65.

Nishimura, Y., Donovan, E., Angelopoulos, V., & Nishitani, N. (2020). Dynamics of auroral precipitation boundaries associated with STEVE and SAID. *Journal of Geophysical Research: Space Physics*, *125*(8), e2020JA028067. https://doi.org/10.1029/2020ja028067

Nishimura, Y., Dyer, A., Kangas, L., Donovan, E., & Angelopoulos, V. (2023). Unsolved problems in strong thermal emission velocity enhancement (STEVE) and the picket fence. *Frontiers in Astronomy and Space Sciences*, *10*, 1087974. https://doi.org/10.3389/fspas.2023.1087974

Nishimura, Y., Gallardo-Lacourt, B., Zou, Y., Mishin, E., Knudsen, D., Donovan, E., et al. (2019). Magnetospheric signatures of STEVE: Implications for the magnetospheric energy source and interhemispheric conjugacy. *Geophysical Research Letters*, *46*(11), 5637–5644. https://doi.org/10.1029/2019gl082460

Nishimura, Y., Yang, J., Weygand, J., Wang, W., Kosar, B., Donovan, E., et al. (2020). Magnetospheric conditions for STEVE and SAID: Particle injection, substorm surge, and field-aligned currents. *Journal of Geophysical Research: Space Physics*, *125*(8), e2020JA027782. https://doi.org/10.1029/2020ja027782

Pavlov, A. (1998). New electron energy transfer rates for vibrational excitation of N_2. *Annales Geophysicae*, *16*(2), 176–182. https://doi.org/10.1007/s005850050591

Puhl-Quinn, P., Matsui, H., Mishin, E., Mouikis, C., Kistler, L., Khotyaintsev, Y., et al. (2007). Cluster and DMSP observations of said electric fields. *Journal of Geophysical Research*, *112*(A5). https://doi.org/10.1029/2006ja012065

Qian, L., Burns, A. G., Emery, B. A., Foster, B., Lu, G., Maute, A., et al. (2014). The NCAR TIE-GCM: A community model of the coupled thermosphere/ionosphere system. *Modeling the ionosphere–thermosphere system*, 73–83.

Radicella, S. M. (2009). The nequick model genesis, uses and evolution. *Annals of Geophysics*, *52*(3–4), 417–422. https://doi.org/10.4401/ag-4597

Ridley, A., Deng, Y., & Toth, G. (2006). The global ionosphere–thermosphere model. *Journal of Atmospheric and Solar-Terrestrial Physics*, *68*(8), 839–864. https://doi.org/10.1016/j.jastp.2006.01.008

Schunk, R. (1977). Mathematical structure of transport equations for multispecies flows. *Reviews of Geophysics*, *15*(4), 429–445. https://doi.org/10.1029/rg015i004p00429

Schunk, R., & Nagy, A. (2009). *Ionospheres: Physics, plasma physics, and chemistry*. Cambridge University Press.

Semeter, J., Hunnekuhl, M., MacDonald, E., Hirsch, M., Zeller, N., Chernenkoff, A., & Wang, J. (2020). The mysterious green streaks below STEVE. *American Geophysical Union: Advances*, *1*(4), e2020AV000183. https://doi.org/10.1029/2020av000183

Southwood, D., & Wolf, R. (1978). An assessment of the role of precipitation in magnetospheric convection. *Journal of Geophysical Research*, *83*(A11), 5227–5232. https://doi.org/10.1029/ja083ia11p05227

Spiro, R., Heelis, R., & Hanson, W. (1979). Rapid subauroral ion drifts observed by atmosphere explorer C. *Geophysical Research Letters*, *6*(8), 657–660. https://doi.org/10.1029/gl006i008p00657

St-Maurice, J.-P., Cussenot, C., & Kofman, W. (1999). On the usefulness of E region electron temperatures and lower F region ion temperatures for the extraction of thermospheric parameters: A case study. *Annales Geophysicae*, *17*(9), 1182–1198. https://doi.org/10.1007/s00585-999-1182-2

St-Maurice, J.-P., & Goodwin, L. (2021). Revisiting the behavior of the E-region electron temperature during strong electric field events at high latitudes. *Journal of Geophysical Research: Space Physics*, *126*(2), 2020JA028288. https://doi.org/10.1029/2020ja028288

St-Maurice, J.-P., & Laneville, P. (1998). Reaction rate of O^+ with O_2, N_2, and no under highly disturbed auroral conditions. *Journal of Geophysical Research*, *103*(A8), 17519–17521. https://doi.org/10.1029/98ja01387

Wright, A. N., & Russell, A. J. (2014). Alfvén wave boundary condition for responsive magnetosphere-ionosphere coupling. *Journal of Geophysical Research: Space Physics*, *119*(5), 3996–4009. https://doi.org/10.1002/2014ja019763

Zettergren, M., Hirsch, M., & Díaz Peña, J. (2024). Geospace environment model of ion-neutral interactions. Version v1.6.1-372-g969ab4ef [Software]. *Zenodo*. https://github.com/jdiazpena/gemini3d

Zettergren, M., & Semeter, J. (2012). Ionospheric plasma transport and loss in auroral downward current regions. *Journal of Geophysical Research*, *117*(A6). https://doi.org/10.1029/2012ja017637

Zettergren, M., Semeter, J., & Dahlgren, H. (2015). Dynamics of density cavities generated by frictional heating: Formation, distortion, and instability. *Geophysical Research Letters*, *42*(23), 10–120. https://doi.org/10.1002/2015gl066806

Zettergren, M., & Snively, J. (2019). Latitude and longitude dependence of ionospheric tec and magnetic perturbations from infrasonic-acoustic waves generated by strong seismic events. *Geophysical Research Letters*, *46*(3), 1132–1140. https://doi.org/10.1029/2018gl081569

Zheng, Y., Brandt, P. C., Lui, A. T., & Fok, M.-C. (2008). On ionospheric trough conductance and subauroral polarization streams: Simulation results. *Journal of Geophysical Research*, *113*(A4). https://doi.org/10.1029/2007ja012532